

Structural, geophysical and petrological investigations of the Sarasåsen intrusion and host rocks, Sveconorwegian orogen, southern Norway

Bjørn Eskil Larsen

Geology Submission date: May 2014 Supervisor: Giulio Viola, IGB Co-supervisor: Håkon Olav Austrheim, UiO

Norwegian University of Science and Technology Department of Geology and Mineral Resources Engineering

Structural, geophysical and petrological investigations of the Sarasåsen intrusion and host rocks, Sveconorwegian orogen, southern Norway.

Bjørn Larsen

Abstract

The Kongsberg terrane consists of amphibolite to granulite-facies ortho- and para-gneisses formed during one or more Mesoproterozoic orogenies, in which the Sveconorwegian orogeny is the most important. The possible existence of a suture zone within the Sveconorwegian belt has been a long-lasting and still ongoing discussion. Here a possible candidate of such a suture zone, the ultramafic Sarasåsen intrusion in the Kongsberg terrane, is investigated by combining field mapping, structural analysis, geochemical and geophysical studies. The study documents that the Sarasåsen intrusion is not affected by high-grade metamorphism and that it post-dates the development of regional tectonic foliation. It is thus interpreted to be a late- to post-Sveconorwegian intrusive event and not part of a suture zone-related ophiolite complex. Field mapping reveal the presence of a major shear zone along the shores of Lake Væleren, named the Væleren Shear Zone (VSZ). The VSZ consists of a steeply dipping sheared foliation and mylonites with south-plunging steep stretching lineations, that are associated with sinistral kinematics. The shear zone has later been affected by large scale steeply plunging isoclinal folding. The mylonitic fabric is cut at a high angle by a lamprophyric dyke that has been dated to 1032 Ma. This age represents a minimum age for the development of the VSZ.

Preface

This thesis was suggested to me by my main supervisor Professor Giulio Viola from NGU/NTNU. I was to be a part of the NGU bedrock team which was mapping the Kongsberg terrane in southern Norway, where I was given an area to map and investigate. It has been a great experience to work alongside the team from NGU both in the field and during the writing process.

I would like to thank the team I worked with in the field: Professor Giulio Viola, Dr. Bernard Bingen, Arne Solli, Espen Torgersen, fellow student Hans Jørgen Kjøll and lastly Professor Håkon Austrheim who joined us from UiO for a couple of days. Your knowledge and experience helped me a lot.

Further I would give additional thanks to Giulio Viola and Bernard Bingen for guiding me through the writing process and giving me helpful feedback along the way. To Håkon Austrheim for letting me use the Electron Microprobe at UiO and providing help to analyse the results. To Espen Torgersen and Thomas Scheiber for giving me a desk at their office and providing many useful discussions.

A big thanks to all fellow students for some good times during the last couple of years. Its been great.

Lastly i would like to thank my family, especially my girlfriend Målfrid, whom I never would have begun this study without.

Contents

Con	itents	•	. iii
Intr	roduction		1
The	e Sveconorwegian Orogen: A review		3
2.1	Lithology of the Sveconorwegian belt		. 3
	2.1.1 Eastern Segment		. 4
	2.1.2 Idefjorden Terrane		. 6
	2.1.3 Bamble and Kongsberg Terrane		. 7
	2.1.4 Telemarkia Terrane		. 8
2.2	A four phase model		. 9
	2.2.1 Arendal phase, 1140-1080 Ma		. 9
	2.2.2 Agder phase, 1050-980 Ma		. 9
	2.2.3 Falkenberg phase, 980-970 Ma		. 10
	2.2.4 Dalane phase, 970-900 Ma		. 12
2.3	Previous work in the Kongsberg terrane		. 12
	2.3.1 Additional work in the area	•	. 16
Met	thodology		19
3.1	Field work		. 19
3.2	Structural investigation		. 20
3.3	Petrographic investigation and geochemistry		. 20
	3.3.2 Effects of serpentinization		. 23
3.4	U-Pb Geochronology		. 24
3.5			
	3.5.1 Quality of data		. 25
	3.5.2 Gridding		. 28
	Int: The 2.1 2.2 2.3 2.3 Me 3.1 3.2 3.3 3.4	Introduction The Sveconorwegian Orogen: A review 2.1 Lithology of the Sveconorwegian belt . 2.1.1 Eastern Segment . 2.1.2 Idefjorden Terrane . 2.1.3 Bamble and Kongsberg Terrane . 2.1.4 Telemarkia Terrane . 2.1.4 Telemarkia Terrane . 2.2.1 Arendal phase, 1140-1080 Ma . 2.2.2 Agder phase, 1050-980 Ma . 2.2.3 Falkenberg phase, 980-970 Ma . 2.2.4 Dalane phase, 970-900 Ma . 2.2.3 Falkenberg phase, 980-970 Ma . 2.3.1 Additional work in the area . 2.3.1 Additional work in the area . 3.3 Previous work in the Kongsberg terrane . 3.1 Field work . 3.3 Petrographic investigation . 3.3.1 Lab work . 3.3.2 Effects of serpentinization . 3.4 U-Pb Geochronology . 3.5.1 Quality of data	The Sveconorwegian Orogen: A review 2.1 Lithology of the Sveconorwegian belt 2.1.1 Eastern Segment 2.1.2 Idefjorden Terrane 2.1.3 Bamble and Kongsberg Terrane 2.1.4 Telemarkia Terrane 2.1 A four phase model 2.1.4 Telemarkia Terrane 2.2 A four phase model 2.2.1 Arendal phase, 1140-1080 Ma 2.2.2 Agder phase, 1050-980 Ma 2.2.3 Falkenberg phase, 980-970 Ma 2.2.4 Dalane phase, 970-900 Ma 2.2.3 Falkenberg phase, 980-970 Ma 2.2.4 Dalane phase, 970-900 Ma 2.3.1 Additional work in the area 2.3.1 Additional work in the area 3.3 Previous work in the Kongsberg terrane 2.3.1 Additional work in the area 3.3 Petrographic investigation 3.3 Petrographic investigation and geochemistry 3.3.1 Lab work 3.3.2 Effects of serpentinization 3.4 U-Pb Geochronology 3.5.1 Quality of data

		3.5.3	Filters	3				
4	Res	ults	3	9				
	4.1	Map de	escription and petrography 3	9				
		4.1.1	Meta-arkose	9				
		4.1.2	Banded Biotite Gneiss	1				
		4.1.3	Mafic granulite	1				
		4.1.4	Leptitic Gneiss 4	2				
		4.1.5	Granitic Gneiss	3				
		4.1.6	Meta-gabbro	3				
		4.1.7	Amphibolite	4				
		4.1.8	Dioritic gneiss	5				
	4.2	Petrogr	caphic investigation and mineral chemistry of the					
		Sarasås	$sen intrusion \dots \dots$	9				
		4.2.1	Leucogabbro	9				
		4.2.2	Serpentinized Peridotite	2				
		4.2.3	Petrology of Sarasåsen intrusion 5	6				
	4.3	Structu	ural framework of the area: a synopsis 5	9				
	4.4	U-Pb C	Geochronology	0				
		4.4.1	Væleren shear zone 6					
	4.5		γ sical investigation					
		4.5.1	Filtering and data enhancement	5				
		4.5.2	Petrophysics	6				
5	Dis	cussion	8	9				
6	Con	clusion	.s 9	3				
-	Ъ			-				
7		1	es and future work 9.					
A	ppen	dices		Ι				
Α	A Samples							
В	Sarasåsen intrusion II							
	B.1	Anhydi	rous Minerals	Ι				

B.2	Hydrous minerals												Х
B.3	Geological Map .				•		•					•	XV

List of Figures

2.1	Tectonic map of the Sveconorwegian orogeny of southwest Scandinavia.	4
2.2	Cumulative probability curves of geochronological data of magmatic events in the four main lithotectonic units of the Sveconorwegian belt (Bingen et al., 2008b)	5
2.3	Sketch maps showing the distribution of metamorphism, magmatic rocks and sedimentary basins during the Sve-	
	conorwegian orogeny.	10
2.4	Map of the Kongsberg terrane, following Starmer (1985)	
	with the area of interest of this study	15
2.5	Map of the Tyristrand - Holleia area (Johannesen, 1974).	17
3.1	Overview of flightlines of the four grids with magnetic anomalies as background	26
3.2	Bouguer anomaly, with measurement points.	30
3.3	Overview of flightlines of the four grids with magnetic anomalies as background.	31
3.4	The effect of terrain clearance on the resolution of geolog- ical detail (Reeves, 2005).	32
3.5	Merged magnetic anomaly	33
3.6	Summary of the mechanics of filtering (Isles and Rankin, 2013).	34
3.7	First vertical derivative visualized	35
3.8	Tilt derivative explained	37
4.1	Lithologic map produced by this study	40

4.2	Thin section micro-photos meta-arkose, meta-gabbro and
	banded biotite gneiss
4.3	Thin section photos of granitic gneiss, mafic granulite and
	amphibolite
4.4	Thin section photos of 1^{st} generation dike and 2^{nd} gener-
	ation dike
4.5	Thin section and electron backscatter images from leuco-
	gabbro
4.6	Thin section and electron backscatter images from serpen-
	tinized peridotite
4.7	Pyroxene, olivine and plagioclase endmembers
4.8	Concordia diagrams
4.9	Stereographic projections from VSZ
4.10	Kinematic indicators from Væleren Shear Zone
	Folding pre-existing stretching lineations
	Photos of 1^{st} and 2^{nd} generation dike hosted in VSZ
	Lineaments drawn from remote sensing
4.14	Low-pass filtered magnetic grid with cut-off wavelength of
	5000 m
4.15	Low-pass filtered gravity grid with cut-off wavelength of
	60 km
4.16	High-pass filtered gravity grid with cut-off wavelength of
	60 km
	THDR of the magnetic grid
	1VD of magnetic grid.
	Analytic signal of magnetic grid
	Positive returns of TDR of magnetic grid
4.21	Samples from investigated area from NGU's petrophysical
	database
5.1	Metamorphic facies in PT diagram
B.1	Geological map of Væleren - Sarasåsen

List of Tables

3.1	Maximum temporal variations allowed. Data provided by the SGU final report on project.	28
3.2	Ground clearance, flightlines spacing (Y) and cell size, with associated Nyquist frequencies and ratio between flight line spacing and ground clearance is listed.	29
		20
4.1	Table showing end members of olivine, plagioclase and pyroxenes.	57
4.2	Wholerock XRF analysis of samples BBI 138 and BBI 139 $$	63
4.3	Petrophysic data from investigated area	86
A.1	Overview of all samples taken and their coordinates in UTM32N	II
B.1	Microprobe analysis from sample BLA-13 (anhydrous minerals)	IV
B.2	Microprobe analysis from sample BLA-14 and BLA-15 (anhydrous minerals)	V
B.3	Microprobe analysis from sample BLA-16 and BLA-17 (anhydrous minerals)	VI
B.4	Microprobe analysis from sample BLA-18, BLA-19 and BLA-20 (anhydrous minerals)	VII
B.5	Microprobe analysis from sample BLA-21 (anhydrous minerals	VIII
B.6	Microprobe analysis from sample BLA-22 (anhydrous minerals)	IX

B.7	Microprobe analysis from sample BLA-13 and BLA-14	
	(hydrous minerals)	XI
B.8	Microprobe analysis from sample BLA-16 and BLA-17	
	(hydrous minerals)	XII
B.9	Microprobe analysis from sample BLA-18, BLA-19 and	
	BLA-21 (hydrous minerals)	XIII
B.10	Microprobe analysis from sample BLA-22 (hydrous minerals))XIV

Chapter 1 Introduction

The Sarasåsen intrusion (Sveconorwegian Orogen, southern Norway) was selected as an interesting target of research because it is known to be one of the very few rock bodies in the whole of the Sveconorwegian orogenic belt to include significant ultramafic rocks. Slivers of ultramafic rocks, representing pieces of ophiolite complexes or slivers of mantle, can be trapped in suture zones in orogenic belt, in particular continent-continent collision zones. Ultramafic rocks can thus potentially provide evidence of paleo suture zones in ancient orogens. The Sveconorwegian orogenic belt does not expose any clear evidence for a Sveconorwegian suture zone. Some of the available orogenic models, however e.g. (Olesen et al., 2004), suggest that large ultramafic bodies exist under the Skagerrak waterway between southern Norway and Denmark. This could be part of an ophiolite complex suggesting that a suture zone exists between the western part of the orogen, called the Telemarkia Terrane, and the eastern part of the orogen. This suture zone could be located along the Bamble and Kongsberg domains, which are characterized by an early Sveconorwegian metamorphism, here called the Arendal phase (Bingen et al., 2008b). In this work, geological mapping, structural analysis, geophysical analysis and petrology were combined to construct a model that explains the origin of the ultramafic Sarasåsen intrusion and its relationship with the regional tectonic setting.

Chapter 2

The Sveconorwegian Orogen: A review

The Sveconorwegian belt is situated in southern Scandinavia. It represents the result of the collision between Fennoscandia and another major continental plate, possibly Amazonia, during the Mesoproterozoic. The Sveconorwegian orogeny is the European counterpart of the Grenvillian orogen, which was a major orogenic event during the assembly of supercontinent of Rodinia. This chapter reviews the tectonic history of the Sveconorwegian orogeny, mainly following the conceptual scheme suggested paper Bingen et al. (2008b). It includes a description of the main units and of the proposed four-phase geological model of the orogeny. A tectonic overview of the orogenic belt is shown in Figure 2.1.

2.1 Lithology of the Sveconorwegian belt

As seen in Figure 2.1 the Sveconorwegian belt consists of four major lithological units, which from east to west, are the Eastern Segment, the Idefjorden Terrane, the Bamble-Kongsberg Terrane and Telemarkia. Those are separated by tectonic contacts expressed by major ductile shear zones with often a long deformation history. The geochronological characterization of the main lithotectonic units is mostly based on magmatic events and Figure 2.2 shows cumulative probability curves of crystalliazation ages for the different units.

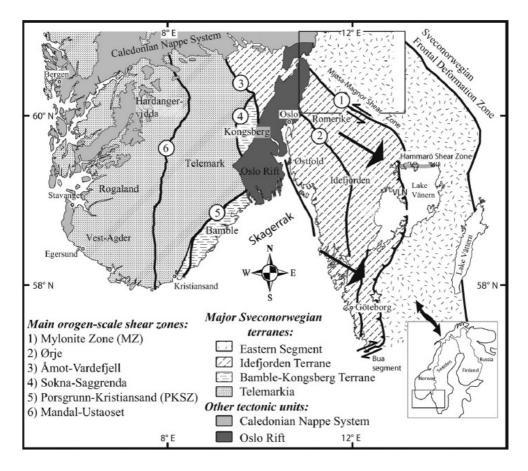


Figure 2.1 – Tectonic map of the Sveconorwegian orogen of southwest Scandinavia. The belt consists of Paleo- to Mesoproterozoic lithologies juxtaposed along major shear zones. Black arrows indicate the transport direction for the "mylonite zone". (Viola et al., 2011)

2.1.1 Eastern Segment

As displayed in Figure 2.2, the Eastern Segment contains rocks with protolith age between 1850 and 1660 Ma (Bingen et al., 2008b). It is mainly made up of granitic gneisses related to the Transcandinavian Igneous Belt (TIB), a belt of igneous rocks in the Fennoscandia foreland, east of the Sveconorwegian orogenic front. The granitic gneisses are intruded by 1560 Ma mafic dykes, 1460-1380 Ma granitic dykes and plutons and 1250-1200 Ma granite plutons e.g. (Söderlund et al., 2002). The segment also contains evidence of pre Sveconorwegian orogenic events. A 1460-

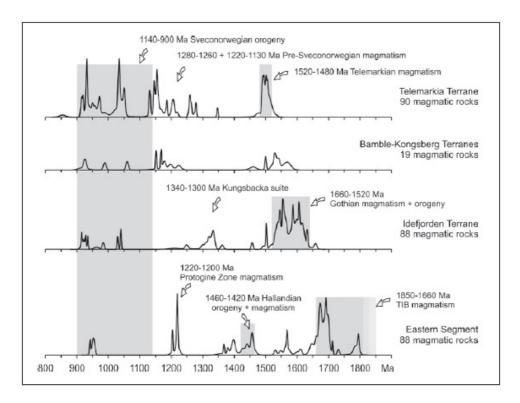


Figure 2.2 – Cumulative probability curves of geochronological data of magmatic events in the four main lithotectonic units of the Sveconorwegian belt (Bingen et al., 2008b)

1410 Ma amphibolite facies metamorphic event the so-called Hallandian event, was recognised by, for example Söderlund et al. (2002). The degree of metamorphism within the Eastern Segment increases to the south and west ((Söderlund et al., 1999); (Bingen et al., 2008b)). In the terrane northern part metamorphism is only recorded close to the Mylonite Zone (Figure 2.1) or local shear zones (Viola et al., 2011). In its southern part, penetrative amphibolite facies metamorphism is widespread with also local occurrences of rocks equilibrated at granulite and even eclogite facies e.g. (Möller et al., 1997). The eastern boundary of the Eastern Segment is defined by the front of Sveconorwegian deformation. It corresponds to the Sveconorwegian Frontal Deformation Zone (SFDZBingen et al. (2008b)). The southern part of the SFDZ merges with the Protogine Zone, which is made up of an extensional shear zone show in Bingen et al. (2008b), Fig 1. The merged zone contains evidence of both reverse and normal top down to-the-east movement. Continuity between the southern parts of the Eastern Segment and the Sveconorwegian foreland is evident on geological maps, suggesting the lack of major displacement along the SFDZ.

2.1.2 Idefjorden Terrane

Two pre-Sveconorwegian magmatic events are constrained within the Idefjorden Terrane. The best represented is the Gothian magmatism between 1660 and 1520 Ma, e.g. (?). The associated plutons and volcanic rocks are mainly calc-alkaline and tholeiitic in composition. From east to the west Gothian lithologies consist of the 1660-1640 Ma Horred metavolcanic sequence, the 1630-1590 Ma Åmål Formation and coeval Gøteborg granite suite, and the 1590-1520 Ma Store Le-Marstrand Formation and coeval Hisingen plutonic suite. The Gothian peak is dated at 1540 Ma and is characterized by amphibolite facies metamorphism (Bingen et al., 2008a). The 1660-1520 Ma lithologies are overlain by a supracrustal package called the Dal group. It is poorly dated but it is intruded by a second magmatic event in the terrane, the 1340-1250 Ma Kungsbacka suite (Austin Hegardt et al., 2007). The supracrustal package is also intruded by post Sveconorwegian norite-granite plutons dating 960-920 Ma (Bingen et al., 2006). The eastern boundary of the Idefjorden Terrane is defined by the Mylonite Zone (MZ), separating Idefjorden from the Eastern Segment ((Viola et al., 2011; Berglund et al., 1997; Johansson and Johansson, 1993; Park et al., 1991; Stephens et al., 1996). It is a sinistral top-to-the-southeast transpressional thrust zone. Though the age of thrusting has not been directly established, zircon U-Pb data from the Idefjorden hanging wall and Eastern Segment footwall indicate ductile deformation between 980 ± 13 and 971 ± 8 Ma (Andersson et al., 2002; Larson et al., 1999). Extensional reactivation of the MZ is also recorded (Berglund et al., 1997; Viola et al., 2011). Indirect measurements have established an age of 917 ± 14 Ma for the extension (Johansson and Johansson, 1993). Dating of biotite and white mica from a mylonitic extensional, greenschist facies reactivated shear zone has also been done by Viola et al. (2011). The analysis yielded biotite ages between 922.6 ± 3.7 and 860.7 ± 5.1 Ma and white mica ages between 912.7 ± 4.1 and 870.2 ± 2.1 , thus constraining a very prolonged phase of regional top-to-the-west extension, commonly associated with the gravitational collapse of the Sveconorwegian belt.

2.1.3 Bamble and Kongsberg Terrane

Magmatic events at 1570-1460 Ma producing mainly calc-alkaline plutonic suites and greywacke dominated metasediments make up the Bamble-Kongsberg terrane. Based on geophysical data (Ebbing et al., 2005), Bamble and Kongsberg have been interpreted as tectonic wedges overlaying the western Telemarkia Terrane. Two metamorphic phases are identified in the terranes. The first one at 1140-1125 Ma is only recorded in the Bamble terrane, and it caused both amphibolite and granulite facies metamorphism. The second, at 1110-1080 Ma, affected both Kongsberg and Bamble. It is also characterized by amphibolite and granulite facies metamorphism conditions in the Bamble Terrane but by metamorphism peak at amphibolite facies in Kongsberg. In fact, data suggest that during the peak of amphibolite-facies metamorphism in the Kongsberg terrane, the Bamble terrane was already experiencing regional cooling and unroofing (Cosca et al., 1998). The boundary between Bamble and Telemarkia is defined by the Porsgrunn-Kristiansand Shear Zone (PKZS (Bingen et al., 2008b), Fig 1). It is defined as a thrust zone that dips towards the southeast. It was also reactivated as an extensional detachment fault (Mulch et al., 2005). Accurate dating of the thrusting has not been done but compressional deformation is thought to postdate the peak of the amphibolite facies metamorphism at c. 1110 Ma. The extensional phase is constrained to 891 ± 14 to 880 ± 3 Ma (Mulch et al., 2005). This is consistent with the late Sveconorwegian cooling between 910 and 860 Ma (Bingen et al., 1998), and the ages reported by (Viola et al., 2011) for the extensional phase accommodated by the Mylonite Zone in Sweden.

2.1.4 Telemarkia Terrane

The oldest identifiable rocks of the Telemark Terrane are dated in the interval between 1520 and 1480 Ma and are referred to as the Telemarkian magmatism. These rocks are felsic orthogneisses (Bingen et al., 2005) interlayered and overlain by a quartzitic metasedimentary sequence older than 1350 Ma (Bingen et al., 2001). Between 1280-1130 Ma these rocks where intruded and unconformably overlain by several magnatic suites and sediments, respectively (Bingen et al., 2002). During the Sveconorwegian orogeny Telemarkia experienced voluminous plutonism, including 1050-1035 Ma granodiorite and granite suites, 1030-1000 Ma syncollisional granitoids, 970-930 Ma post-collisional monzodiorite to granite plutons and the 930-920 Ma Rogaland anorthosite-mangerite-charnockite (AMC) complex (Duchesne et al., 1985; Demaiffe et al., 1986; Schärer et al., 1996; Schiellerup et al., 2000; Andersen et al., 2001; Bogaerts et al., 2003; Vander Auwara et al., 2003). The Telemarkia Terrane is divided into four "sectors". These are the Telemark in the east and in the west Hardangervidda, Suldal and Rogaland-Vest Agder (RVA) sectors from north to south.

The Hardangervidda sector consists of amphibolite facies gneisses. They are characterized by a general E-W oriented foliation (Sigmond, 2003). The Suldal sector consists mainly of greenschist to epidote-amphibolite facies supracrustal sequences, and plutonic rocks. The metamorphism in both sectors is believed to be pre-Sveconorwegian. The central parts of the Telemark sector consist of supracrustal rocks, which still preserve the original stratigraphic relationships. The metamorphic grade increases to the northeast of the sector up to amphibolite facies, while the central parts only contain lower-grade metamorphism. The southern parts of the sector also contain amphibolite facies rocks. The age of this metamorphism (c. 913 Ma) attests to a late Sveconorwegian high-grade metamorphism (Bingen et al. 1998). The Rogaland-Vest Agder sector contains high grade metamorphism, from amphibolite to granulite facies. There is an increase in metamorphism towards the southwestern AMC complex. Recent studies concluded that a deformation event younger than 917 ± 3 Ma took place in this sector, and ductile deformation is recorded in postcollisional plutons (Bolle et al., 2000). The western boundary of the

Telemark sector is defined by the N-S trending Mandal-Ustaoset Fault and shear zone(Bingen et al. (2008b), Fig 1). The eastern boundary is also the boundary of the Telemarkia and Idefjorden terranes. It dips to the southwest and is characterized by amphibolite facies banded gneiss rich in amphibolite-layers and amphibolite boudins. The timing of the metamorphism is coeval or younger than Sveconorwegian peak metamorphism at c. 1010 Ma. Studies have shown extensional deformation at 985 ± 5 Ma (Bingen et al., 2008a). No late orogenic extensional deformation is recorded after 985 Ma.

2.2 A four phase model

Based on metamorphic and magmatic ages a four phase model of the Sveconorwegian orogeny has been developed and proposed by Bingen et al. (2008b). The four phases are the Arendal, the Agder, the Falkenberg and the Dalane phase (Figure 2.3).

2.2.1 Arendal phase, 1140-1080 Ma

Pre Sveconorwegian closing of an oceanic basin caused northwest-directed subduction of the Idefjorden under Telemarkia. This led to the creation of the 1180 Ma Tromøy volcanic arc, now accreted to the Bamble Terrane. The tectonic wedge consisting of Kongsberg and Bamble was created during peak metamorphism at c. 1140 Ma, during the collision between Idefjorden and Telemarkia. Thrusting during 1140-1080 Ma was followed by regional cooling. Clastic sediments deposited after 1120 Ma in the Telemark sector as a part of a foreland or an intromontane basin are probably related to mountain building and denudation. Between 1080 and 1050 Ma there was a period of tectonic inactivity in the Sveconorwegian belt.

2.2.2 Agder phase, 1050-980 Ma

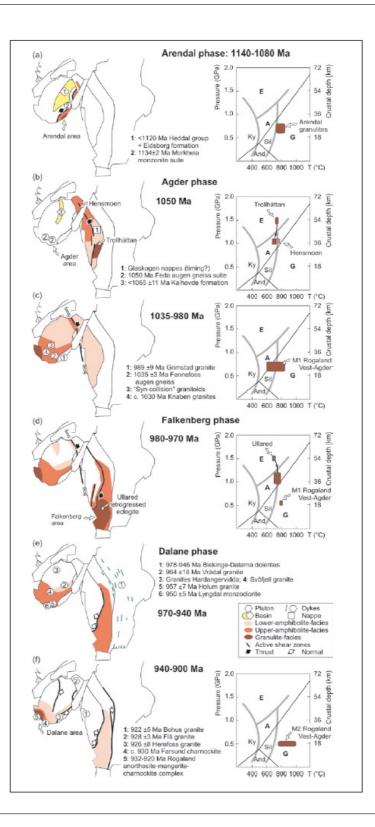
The Agder phase represents the most pervasive tectonic event of the Sveconorwegian orogeny. Fennoscandia and another large continent, possibly Amazonia, collided in an oblique continent-continent collision. During the collision, the Idefjorden was underthrust and buried to a depth that could have exceeded 50 km. Eastward thrusting along major shear zones in Idefjorden are possibly coeval with this event. Telemarkia entered a period of crustal thickening at 1035 Ma. Metamorphic data suggest that lithologies of the RVA sector resided under high-grade metamorphic conditions for over 100 My between 1035 and 900 Ma. Metamorphism peaked in granulite facies during the Agder phase between 1035 and 980 Ma. During this time of crustal thickening in Telemarkia, the Idefjorden Terrane experienced unroofing at 1025 Ma. This suggests exhumation of high-pressure metamorphic rocks still in a convergent setting. Deformation during collision was possibly accommodated by the Vardefjell Shear Zone between 1010 Ma and 985 Ma, with thrusting towards northeast (Figure 2.1). This period is coeval with peak metamorphism in the Telemarkia hanging wall, but post-dates exhumation of high pressure rocks in the Idefjorden footwall.

2.2.3 Falkenberg phase, 980-970 Ma

During this period crustal thickening had propagated eastwards. Highgrade metamorphism as high as eclogite facies, dated at 972 ± 14 Ma is recorded in the Eastern Segment. This was followed by exhumation to middle crustal levels (Möller et al., 2007). The Mylonite Zone was active during this period and accommodated SE thrusting of the Idefjorden Terrane onto the Eastern Segment. In the RVA sector of the Telemarkian Terrane, the Falkenberg phase is considered the transition period between convergent and divergent tectonics.

Figure 2.3 (facing page) – Sketchmaps showing the distribution of metamorphism, magmatic rocks and sedimentary basins during the Sveconorwegian orogeny. For each time slice, metamorphism is illustrated in the pressuretemperature space. From (Bingen et al., 2008b).

- (a) Arendal phase: 1140-1080 Ma.
- (b, c) Agder phase: 1050-980 Ma.
- (d) Falkenberg phase: 980-970 Ma.
- (e, f): Dalane phase: 970-900 Ma.



2.2.4 Dalane phase, 970-900 Ma

After 970 Ma convergent tectonics subsided and the Sveconorwegian belt entered a period of gravitational collapse. The lack of a preserved foreland basin suggests that thinning of the belt was driven by extension over erosion. As a result of exhumation of high-grade domains in the southern part of the Eastern Segment and the RVA sector in Telemarkia, two large-scale gneiss domes were produced (Bingen et al., 2006). The dome in the Eastern Segment is exhumed in the footwall of the Mylonite Zone (Viola et al., 2011). Studies by Möller et al. (2007) show that the rapid exhumation in the footwall formed high-strain zones caused by N-S directed shortening and E-W extension through crustal flow. Exhumation subsided and regional cooling occurred between 960 and 920 Ma in the Eastern Segment. The period of exhumation overlaps with the formation of N-S trending, steep normal shear zones in the Protogine zone at the front of the orogen. The doming in the RVA sector of the Telemarkia Terrane can be divided in two stages. A first stage at 970-940 Ma was associated with voluminous plutonism as a result of decompressional melting during exhumation (Auwera et al., 2003). Regional structural patterns suggest N-S directed extension. A second stage at 930-910 Ma was restricted to the southwest of the RVA sector and is associated with the intrusion of the 930-920 Ma Rogaland AMC suite. This was followed by regional cooling between 920 and 900 Ma. Studies suggest that central parts of the Sveconorwegian orogen, the Telemarkia and Idefjorden Terrane, show little unroofing during the Dalane phase. Brittle crustal conditions and extensional settings are registered between 970 and 910 Ma (Hellström et al., 2004). Extensional reactivation of major Sveconorwegian shear zones occurred between 970 and 880 Ma (Scherstén et al., 2004).

2.3 Previous work in the Kongsberg terrane

Extensive work was done in the Kongsberg terrane by Starmer in the 70's and 80's. This section will summarize his work, with special reference

to Starmer (1985), where several episodes of metamorphism and faulting are described. There are two major orogenic episodes described. The earliest is referred to as the Kongsbergian (hereafter named Gothian) orogeny at c. 1600 - 1500 Ma (Oftedahl, 1980; Starmer, 1977; Jacobsen and Heier, 1978). The Sveconorwegian orogeny (c. 1300 - 1000 Ma) is the second event.

The Kongsberg terrane is divided into three natural divisions (Starmer, 1985). The West Kongsberg Complex (WKC), the Modum Complex (MC) and the East Kongsberg Complex (EKC). They are separated by pre-Sveconorwegian large-scale folding. The shear zones that now separate the complexes are introduced later. There are three major mylonite zones that can be identified in the Kongsberg Terrane. They are the Saggrenda-Prestfoss mylonite zone (SPMZ), the Prestfoss-Sokna mylonite zone (PSMZ) and the Hokksund-Solumsmo mylonite zone (HSMZ). The first two form the western border of the Kongsberg terrane to Telemarkia (together called Sokna-Saggrenda). The HSMZ was formed when the Modum Complex was thrust obliquely onto the West Kongsberg Complex (Starmer, 1985). In addition to the major shear zones there are several smaller shear zones throughout the Kongsberg terrane.

The major shear zones also show evidence of brittle reactivation (Starmer, 1985). The most significant, labelled the "friction breccia" (Bugge, 1928), reflects the partial reactivation of SPMZ and PSMZ. It runs along the length of the entire terrane and downthrows the Kongsberg terrane relative to Telemarkia with a normal displacement. Displacement increases from north to south. The HSMZ is also brittlely reactivated. The western side was downthrown with increasing displacement to the north (Starmer, 1985). These two faults could be a part of a conjugate set of extensional N-S striking normal faults. In addition to the reactivation to these two N-S striking shear zones there are several E-W trending faults, the Simoa fault and a set of north dipping normal faults north of the EKG, between Hønefoss and the Ådal granite (Figure 2.4).

Starmer's interpretation of the evolution of the Kongsberg terrane

Starmer (1985) separates up to six individual phases of ductile deforma-

tion between c. 1600 and 1000 Ma. The first deformation at c. 1600 involved E-W compression and establishment of subvertical N-E striking foliation and mylonites. The SPMZ shear zone nucleated at that time. It also created major north dipping folds, which separate the WKC, MC and EKC. Prior to the next phase of ductile deformation, granitic bodies intruded at about 1550 - 1520 Ma (Starmer, 1985). The second ductile phase created foliation and minor shear zones in the intruded granites. This event was followed by mafic to intermediate magmatism at c. 1500 Ma, before a third phase of ductile deformation occurred. All three deformation events happened at upper amphibolite to granulite metamorphic facies condition during the orogeny Starmer labelled Kongsbergian, which is now known as the Gothian orogeny.

The fourth episode of ductile deformation took place at c. 1250 Ma (Starmer, 1985) and marked the beginning of an early phase Sveconorwegian orogeny. During this event, the SPMZ and PSMZ thrust the Kongsberg terrane NW onto Telemarkia. The HSMZ was developed when the MC was thrust NW developing $60-70^{\circ}$ south plunging lineations on steeply dipping foliation planes. The fifth episode of ductile deformation accommodated the same compressional tectonics as the fourth and it caused further strain accommodation along the shear zones on the western margin of Kongsberg terrane.

After a quiescent period, a second phase of the Sveconorwegian Orogeny (not to be confused with the four phase model from Bingen et al. (2008b)) started with the sixth and final episode of ductile deformation (Starmer, 1985). It involved only local ductile thrusting and buckle folding. Only narrow mylonite zones were created during this event. This was followed by a pure shear metamorphic climax at c. 1060 Ma with crystallized garnets overprinting mylonitic fabric (Starmer, 1985). This phase of Sveconorwegian orogeny peaked at mid amphibolite facies.

Starmer (1985) concludes that most major fold structures and ductile deformation events in the Kongsberg terrane can be ascribed to the Gothian orogeny. Peak metamorphism was also reached during this episode (Gothian peaked in granulite and Sveconorwegian in mid amphibolite metamorphic facies).

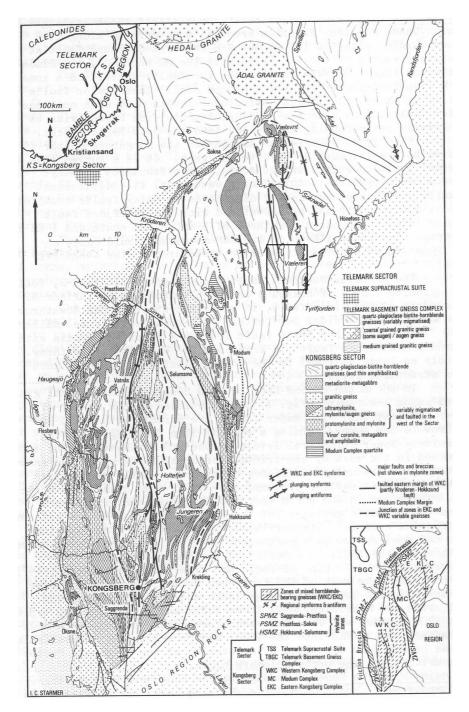


Figure 2.4 – Map of the Kongsberg terrane, following Starmer (1985) with the area of interest of this study.

2.3.1 Additional work in the area

In addition to Starmer work a MSc thesis done by Johannesen (1974) covers the area of interest. Johannesen focused on the mineralizations around Tyristrand and Holleia and also produced a lithological map (Figure 2.5).

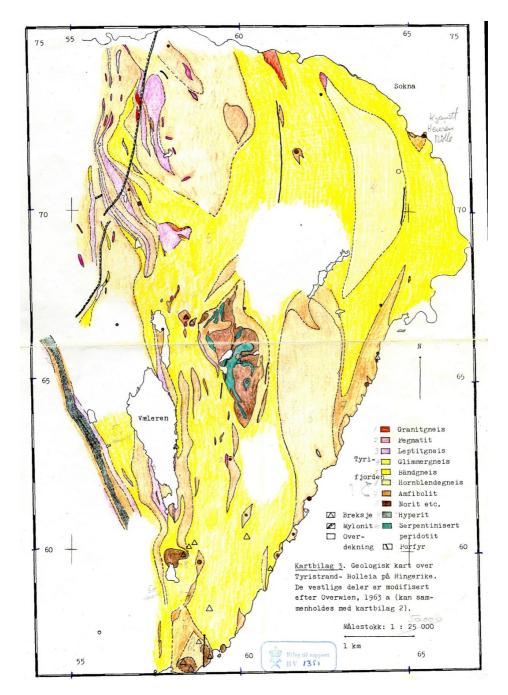


Figure 2.5 – Map of the Tyristrand - Holleia area (Johannesen, 1974).

Chapter 3

Methodology

3.1 Field work

I spent several weeks in the field mapping the area over a two year period. The mapping was done digitally using the ESRI ArcSuite on a portable Panasonic ruggedized "Toughbook", with an integrated GPS unit. The SIGMA plugin for ArcMap developed by the British Geological Survey (BGS) allowed easy and precise localization of outcrops and a powerful system for recording georeferenced notes, pictures, samples and measurements. Bringing a portable tablet to the field also provided an advantage since it allowed easy access to already published geological maps and the results of high-resolution airborne geophysical surveys recently acquired by the BGU. In addition to the geological maps, it was thus possible to refer to modern, high-resolution, geophysical data including gravimetric, magnetic and EM grids was brought. Detailed topographic maps based on Kartverket 10m resolution digital elevation models (DEM), and a limited area LiDAR derived digital terrain model (DTM) model which provided a high resolution terrain model with vegetation removed. This allowed very detailed remote sensing of surface lineaments. Having access to all these different information sources in the field, allowed to make early on-the-fly interpretations. However these interpretations were easily expanded or discarded as field investigations went on. Also, when dealing with ancient rocks age (1 Ga - 1.5 Ga), magnetic remanence due to many polarity shifts in the earths magnetic field can cause magnetic anomalies to change in direction and/or intensity depending on present day magnetic field in relation to remanent magnetic field preserved in the investigated rocks. This can result in a mismatch between displayed anomalies and anomaly source. To rectify this, the remanent magnetism would have to be measured from oriented samples taken from the entire area. This was not done in this investigation, such that the location of magnetic highs and lows could have shifted.

3.2 Structural investigation

At every locality lithology, structural observations and measurements, a general description of the locality and sometimes photos and sketches were taken to provide as detailed of a description as possible. Of all structural observations made the most dominant feature was the pervasive N-S striking regional foliation. The only lithology that did not show this foliation was the ones hosted by the Sarasåsen intrusion which, is instead characterized by planar anisotropies more reminiscent of primary magmatic features (see below). Shear foliation with associated stretching lineations was separated from the regional foliation. Brittle fault planes with associated striations were also mapped. Axial planes and fold axis were consistently measured. All structural data was processed using stereographic projection. In order to describe and reduce the data several stereonets were produced with regards to structure type and geographic location.

3.3 Petrographic investigation and geochemistry

During field work 19 samples were collected in 2013 and 24 samples in 2012. Thin sections were made of all 43 samples. Three samples were also dated by U-Pb on zircon. Polished thin sections were made from all samples taken from the Sarasåsen intrusion. This was done in order to study these samples with an electron microprobe. All samples were also studied in a polarized light microscopy in order to produce petrographic

descriptions.

3.3.1 Lab work

Polished thin sections were made from samples BLA-13 through BLA-22. These samples were taken from a 100 m long profile line in the Sarasåsen intrusion. Analyses were done in WDS mode on a Cameca SX100 microprobe at the University of Oslo (UiO) with the following specifications: accelerating voltage: 15 kV Beam current: 15 nA - focused electron beam, counting time on peak: 10 s. Used calibration standards (natural and synthetic) were wollastonite (Ca, Si), Al_2O_3 , metal Fe, pyrophanite (Ti, Mn), Cr_2O_3 , NiO, MgO, albite (Na), orthoclase (K). Na and K were analyzed first.

A total of 160 points were analysed. All analyses are available in the appendix section. The data were then processed and reduced. The first step of reduction was to derive mineral formulas for all analysed points. When calculating formulas for olivine and plagioclase the method presented in by Deer et al. (1992) was applied (Appendix 1). For olivine the number of cations was calculated on the basis of all iron being Fe^{2+} and the number of oxygens was normalized to 4. The same method was applied to plagioclase except the number of oxygens was normalized to 8. End member calculations were also done. The olivine endmembers are forsterite (Fo) and fayalite (Fa). The plagioclase endmembers are anortite (An), albite (Ab) and orthoclase (Or).

Since pyroxenes can contain both Fe^{2+} and Fe^{3+} a different approach was followed to calculate their chemical formula. Since the raw data from the microprobe comes with the assumption that all iron is Fe^{2+} it is necessary to estimate how much of the iron actually is Fe^{3+} . A spreadsheet produced by Prof. Robinson at NGU that calculates this based on the ideal number of cations, which is 4 in the case of pyroxene, was used. It works under the assumption that iron is the only element present with variable valency and oxygen is the only anion. Further the spreadsheet assigns the cations to either T, M1 or M2 sites, making out the structural formula M2M1T₂O₆. The calculated pyroxene endmembers were enstatite (En), ferrosilite (Fs) and wollastonite (Wo), with the Fs component including Fe^{2+} , Fe^{3+} and Mn. When calculating the formulas for pumpellyite, prehnite, talc and serpentine there is also H_2O to be accounted for. Since this does not show on the microprobe results, a workaround has to be applied. The one used in the case of serpentine was to assume 5 oxygens plus 4(OH) in the formula, and calculate the cations based on 7(O). In the case of talc 20 oxygens plus 4(OH) were assumed, and cation calculations were based on 22(O). The number of calculated cations in pumpellyite 17(O) was based on 12(O) and the number of calculated cations in prehnite was based on 11(O).

As amphiboles are very complex and difficult to classify, a spreadsheet published by Leake et al. (1997) were used to calculate cations and classify all amphiboles. The spreadsheat classification is based on the chemical contents of the standard amphibole formula $AB_2^{VI}C_5^{IV}T_8O_{22}(OH)_2$. The ions that normally occupy these sites are

А	(Empty site) and K
A or B	Na
B only	Ca
C or B	L-type ions, commonly Mg, Fe^{2+} and Mn^{2+}
C or T	M-type ions: Al
C only	M-type ions: Fe^{3+} , (rarely Mn^{3+} and Cr^{3+}
C or T	High valency ions: Ti ⁴⁺ ,
C only	Zr^{4+} and
T only	Si
at OH	Anions: O, OH, F and Cl

Based on these assumptions the spreadsheet calculates standard amphibole formulas as follows: If H₂O content is unknown the formula is calculated on the basis of 23(O). Then the T site is summed up to 8 using Si, then Al, the Ti. C site is summed to 5 using excess Al and Ti from T site, and the successively Zr, Cr^{3+} , Fe^{3+} , Mn^{3+} , Mg, Fe^{2+} , Mn^{2+} , any other L²⁺-type ions, and then Li. Then B is summed to 2 using excess Mg and Fe^{2+} , Mn^{2+} and Li from C site, then Ca and Na. Excess Na is assigned to A site then all K.

3.3.2 Effects of serpentinization

Serpentinites consist of the serpentine-group mineral lizardite antigorite and chrysotile. They are formed by low temperature hydration of peridotites where the Mg-rich minerals olivine and orthopyroxene are replaced by serpentine (Evans et al., 2013). The structure formula of serpentine is approximately $Mg_3Si_2O_5(OH)_4$.

Lizardite is the most common form of serpentine. Its structure is layered and it is usually formed by retrograde metamorphism and is most stable at lower temperatures compared to the other serpentines (between 200 and 300°C and at 70 MPa; Grauby et al. (1998). It is also common that Al and Fe³⁺ are substituted for Mg and Si in lizardite.

Antigorite has, similar to lizardite a layered mineral structure, but the layers are more strongly bonded together. This means that antigorite lacks the cleavage that is common in lizardite (Evans et al., 2013). Like lizardite, antigorite contains Al and Fe^{3+} and is also enriched in Si. However, antigorite is associated with prograde metamorphism and is considered to be a high temperature and pressure phase of serpentine.

Chrysotile is different than the other serpentines with a fibrous structure. It is more stable than lizardite at temperatures above 400°C and is usually found in recrystalized or metamorphosed serpentine (Evans et al., 2013). Chrysotile is poor in Al and Fe and is usually found in fractures cutting serpentines (Evans et al., 2013).

Volume changes

There are two conceptual end members to consider with regards to volume changes during serpentinization. One end member is that the mass balance is stable and therefore volume increase is necessary in order to accommodate the serpentine crystallization. Potential volume increase could then be as large as 40% (Evans et al., 2013). The other end member is isovolumetric serpentinization. This means that no expansion occurs during serpentinization due to depletion of major elements. However studies by O'Hanley (1996), and Hattori and Guillot (2007) suggest that whole-rock major element depletion does not happen.

Studies by Steiger (2005) show that the recrystallization pressure ex-

erted by the growing serpentine mineral could range from 20 to 100 MPa depending on fluid properties. Investigation of thin sections from Sarasåsen intrusions reveals fracturing of interstitual plagioclase surrounding serpentinized olivine.

3.4 U-Pb Geochronology

U-Pb geochronological data were collected on zircon from three samples in the map area, as part of mapping program of the Geological Survey of Norway (NGU) in the Kongsberg terrane. Zircon was separated after crushing the samples. Classical methods of heavy mineral separation were used, mainly density separation using a water table and heavy liquids and magnetic separation using a frantz isodynamic sparator. Zircon crystals where hand picked under alcohol under the binocular microscope. Selected crystals were mounted in epoxy together with chips of the reference zircon, and polished to approximately half thickness. The zircons were imaged individually with a panchromatic cathodoluminescence (CL) detector and a backscattered electron detector in a variable pressure scanning electron microscope at the NGU. Geochronological data were collected by Secondary Ion Mass Spectrometry (SIMS) with the Cameca IMS 1280 at the NORDSIM laboratory, Swedish Museum of Natural History in Stockholm. Data were acquired by B. Bingen under supervision of the NORDSIM staff. Analytical protocols and data reduction follow Whitehouse et al. (1999) and Whitehouse and Kamber (2005). Analyses were performed with a primary beam of ca. 15 μ m in diameter, and were calibrated using the 91500 Geostandard reference zircon (1065 Ma, Wiedenbeck et al. (1995), measured at regular intervals. The analyses are corrected for common Pb using the 204Pb signal, if this signal is above background. Decay constants are those of Jaffrey et al. (1971). Age calculations and concordia diagrams (Ludwig, 1998) were prepared with the ISOPLOT macro for XL (Ludwig, 2001). Data are plotted in inverse (Tera-Wasserburg) concordia diagrams. All calculated uncertainties are quoted at 2 sigma in the text (with propagation of decay constant uncertainties).

3.5 Geophysical Investigation

This section describes the reduction, analysis and interpretation of magnetic and gravity surveys of the Tyristrand area. The magnetic survey covers the western part of Tyrifjorden. The gravity survey covers an area stretching across the Oslo-graben. This area is dominated by felsic intrusions and early Paleozoic sedimentary rocks.

3.5.1 Quality of data

In order to produce a grid from a set of data points, interpolation between data points must be performed. The acquisition of data therefore has to be done in such a way that interpolation errors are minimized. This section will describe the acquisition of both magnetic and gravity data, and asses their quality.

Since the magnetic grid used for interpretation is stitched together from four smaller grids, a section of grid stitching will also be presented.

Magnetic and Gravimetric Surveys

The magnetic dataset used in this project is divided in four datasets, and was acquired by different companies. The grids are labelled A through D, with A representing the westernmost and D the easternmost grid, (Figure 3.1). Survey A and D were acquired by the Geological Survey of Sweden (SGU) on on contract for the Geological Survey of Norway (NGU), survey B was flown by Fugro Airborne Surveys for their client A/S Sulfidmalm while it is not known who flew survey C. The lack of metadata has unfortunately affected the reduction of the magnetic field data and, in turn, also the stitching of the four grids.

Magnetic Survey A The survey was acquired by helicopter flown at an altitude averaging 72 m above ground. Flight lines were flown in an E-W direction with an average length of 10 km and a sampling interval of 5 m along flight lines. Distance between flight lines was ca 200 m. There is no information to allow for corrections of temporal variations with the dataset. The database includes a channel for base-station readings every

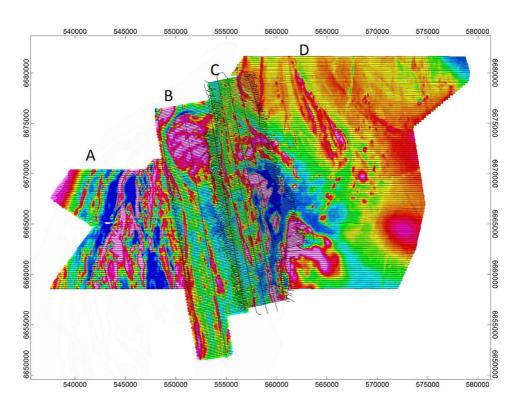


Figure 3.1 – Overview of flightlines of the four grids with magnetic anomalies as background

 $3^{\rm rd}$ minute (roughly 75 m). The entire survey was flown without tie-lines. An IGRF correction has also been applied. No further processing was therefore done on this dataset.

Magnetic Survey B All information on flight lines and corrections presented on Grid B is based on the content of the database. The dataset did not provide meta data on survey specifics or corrections made, only date of measurements and coordinates system with projection method. The orientation of the flight-lines is roughly 080 and not the standard E-W direction often used to cut perpendicularly the direction the earths magnetic field. This is probably done so that flight lines were perpendicular to the regional strike of the foliation. Distance between flight-lines has been measured to an average of 150 m, with sampling interval of 4 m and length of 5.7 km. A channel in the database, "ALTIBIRDM", was

interpreted to be terrain clearance. It ranges from 20 m to 183 m with an average of 46 m, including tie lines. A total of three tie lines has been flown, with a distance of 2.6 km between them. Their length is 25 km for the two eastern lines and 21 km for the western one. All three have a sampling interval of 4 m, as in the case of flight lines.

To eliminate temporal variations, in addition to tie-line levelling, base station readings has been applied to calculate diurnal variations. No removal of IGRF had been done with the data. Calculation of earth field was done with Oasis Montaj, using DGRF values for each reading coordinate at an altitude of 200 m above sea level and date provided by survey data.

Magnetic Survey C No meta-data was provided for this dataset. All information is based on the database content. The orientation of the flight lines is identical to that of Grid B, but the resolution is better. The distance between flight lines is 100 m, with a sampling interval of 4 m and a length varying between 5 and 7 km. Five tie-lines were flown with a distance of 1 km and the sampling density is identical to that of the flight-lines. There is no data available on flying height or date of production. This affects the IGRF removal, but the same values as IGRF calculation of grid B were applied. From base station readings diurnal effects had been corrected for by the surveying company.

Magnetic Survey D The survey was flown by helicopter in September 2009 by the SGU. Flight lines are oriented E-W with line spacing of 200 m, and they were flown at an altitude averaging 77 m. Flight line length varies but averages 15 km, with sampling interval of 10 m. The survey, as in the case of survey A, was carried out without the use of tie lines. Two base stations were used during sampling, one in Skien and one in Kongsberg. The data was processed by the SGU, including diurnal variations, IGRF removal and microlevelling confined to 3 nT. SGU also applied the following quality control of the data (Table 3.1):

Gravimetric Survey The data is from the NGU database. It was collected manually on the ground by deploying portable gravimeters. The

Distance l	between basestation a	nd helicopter
Less than 50 km $$	Between 50-100 $\rm km$	Between 100-150 $\rm km$
15 nt/2 minutes	12 nT/2 minutes	10 nT/2 minutes
35 nT/10 minutes	25 nT/10 minutes	15 nT/10 minutes
100 nT/ hour	70 nT/ hour	50 nT/ hour

Table 3.1 – Maximum temporal variations allowed. Data provided by the SGU final report on project.

distance between measurements varies throughout the area, ranging from less than 1 km up to 6 km. Free-air and bouguer corrections have been applied.

3.5.2 Gridding

Magnetic Grids

When conducting a survey, the key elements are a sufficient number of readings in the x and y direction and the flying altitude. The detail of the data is limited to the Nyquist wavelength N = 2d, where the N is the shortest wavelength that is possible to measure given a sample interval of d at a given measuring altitude. In gridded data "d" is the cell size. This makes flightline line spacing very important. It can be argued that in the case of the area discussed here, the surveys are oriented in such a way that most changes in geology occurs along flightlines, ie perpendicular to strike of lithologies, making the flightline spacing less important. But it should be kept in mind that anomalies between flightlines has to be considered as possible artefacts.

Looking at Table 3.2, the minimum wavelength along flightlines varies between 10 m and 20 m, however across flightlines no wavelength below 200 m is possible to measure. This means that a source with wavelength less than 200 m will not be visible along the N-S direction.

Also, the minimum wavelength along the flightlines varies between 10 m and 20 m, however across the flightlines it is not possible to measure any wavelength below 200 m. This means that a source with wavelength less than 200 m will not be visible along the N-S direction.

	Survey A	Survey B	Survey C	Survey D
Ground clearance, S	72 m	46 m	Unknown	$77 \mathrm{m}$
Spacing Y	$200 \mathrm{m}$	$150~\mathrm{m}$	$100 \mathrm{~m}$	$200 \mathrm{m}$
Cell Size	$50 \mathrm{m}$	$50 \mathrm{m}$	$50 \mathrm{m}$	$50 \mathrm{m}$
Nyquist Y	$400 \mathrm{m}$	$300 \mathrm{m}$	$200 \mathrm{~m}$	400 m
Nyquist Cell	$100 \mathrm{~m}$	$100 \mathrm{~m}$	$100 \mathrm{~m}$	$100 \mathrm{~m}$
Ratio Y/S	2,8	$3,\!3$	Unknown	2,6
Year of aquisition	Unknown	Mar 2006	Unknown	Sept 2009

Table 3.2 – Ground clearance, flightlines spacing (Y) and cell size, with associated Nyquist frequencies and ratio between flight line spacing and ground clearance is listed.

The ground clearance also causes a problem when gridding the data. To avoid undersampling, a ratio of 1:1 between ground clearance and flight line spacing is optimal. However in order to achieve sufficient geological detail, ground clearance should be kept to a minimum. It is important to notice that undersampling across flightlines will increase as the ratio between line spacing and flying height increases. Isles and Rankin (2013) suggest a ratio of 4:1 is tolerable but should not be exceeded. As seen in Table 3.2 none of the surveys exceeds this ratio (except maybe Survey C which is unknown), but with a ratio of more than 2.5 some undersampling across flightlines will be expected.

A cell size of 50 m was chosen when gridding that data. This was according to the 1/4 ratio of cell size and line spacing suggested by Isles and Rankin (2013). A lower cell size would reveal too many flightline-perpendicular artefacts.

Gravity Grid

The distance between measurements varies throughout the dataset, from 100 m to 6000 m. This gives Nyquist wavelengths from 200 m to 12000 m. A grid cell size of 2500 m was chosen. If larger size is applied resolution of detailed areas are lost, and smaller cell size creates more artefacts due to undersampling. This gives Nyquist wavelength of 5000 m, making the gravity survey unsuitable for analysing the shallow subsurface.

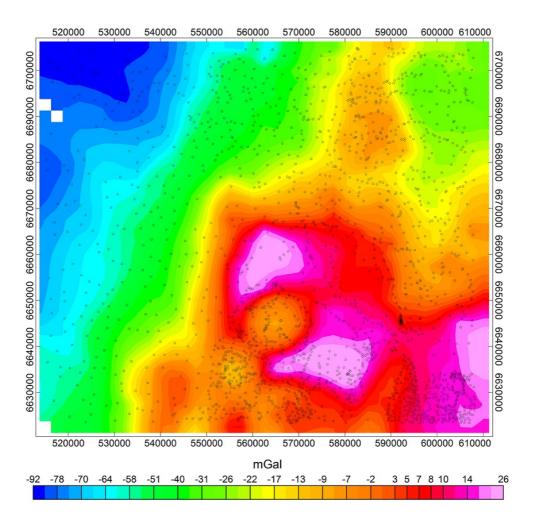


Figure 3.2 – Bouguer anomaly, with measurement points.

Merging Magnetic Grids

In order to merge the four available grids into one large single grid, the dataset had to be levelled to avoid artefacts along borders and a shift in intensity. Figure 3.3 displays an overview of the difference between the four grids where they overlap. A comparative analysis of the three overlapping zones reveals that the difference between A and B is the highest. Grid A has values ca 200 nT lower than Grid B in the overlapping area. Most likely this is caused by the different ground clearance of the two surveys. Grid A was flown at an average altitude of 72 m whereas Grid

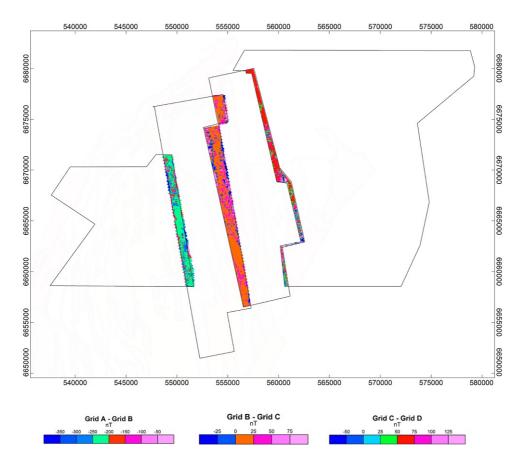


Figure 3.3 – Overview of flightlines of the four grids with magnetic anomalies as background.

B at an average altitude of 46 m. As seen in Figure 3.4 a difference in intensity of 200 nT can easily be achieved with 30 m difference in flying altitude.

The difference between Grid B and C is more subtle. However there seems to be two zones within the overlapping area. In the south the difference is mainly in the orange field (0 to 25 nT) and in the north both in the purple (25 to 50 nT) and blue (-25 to 0 nT), ie the northern part has both lower and higher differences. This could be due in part to different IGRF correction values, although this would only explain the change from low to high toward the north and not the small difference in the northern part of the surveys. The other changes could be due to one

of the surveys being more detailed, thus providing anomalies where the other less detailed survey does not. Both datasets came without removed IGRF field. But since only Survey B specifies the date for its acquisition and C does not, it is expected that the shift in difference in field intensity will shift along latitude.

The difference between Grid C and D also seems to follow a regional trend that ranges from 50 - 75 nT in the north and a more mixed variation in the south. The mixed variation in the south coincides with a prominent magnetic high. This mixed zone seems to be created by the difference in resolution of the two grids. While Grid D treats the magnetic high as a high wavelength anomaly, Grid C has more detail and reveals a number of short wavelength anomalies in addition. The unknown date of survey C probably also caused a shift from north to south because of IGRF removal, but this is not visible.

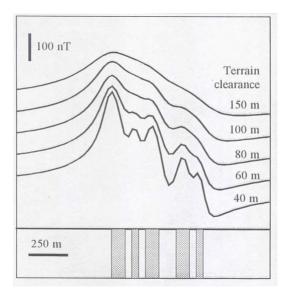


Figure 3.4 – The effect of terrain clearance on the resolution of geological detail (Reeves, 2005).

Based on the available information, Grid B was chosen as the static grid when merging. The quality of Survey B and C are both high, but lack of information for Survey C caused B to be preferred. Survey A and D are of lower quality and were flown without tie-lines and are therefore not suited to be used as reference grid which all other grids are levelled to. First Grid A and B were merged and Grid A was raised to B. Grid AB was then merged with Grid C with AB as the static grid. Lastly Grid ABC was kept static while it was merged with Grid D. The final merged grid is shown in Figure 3.5.

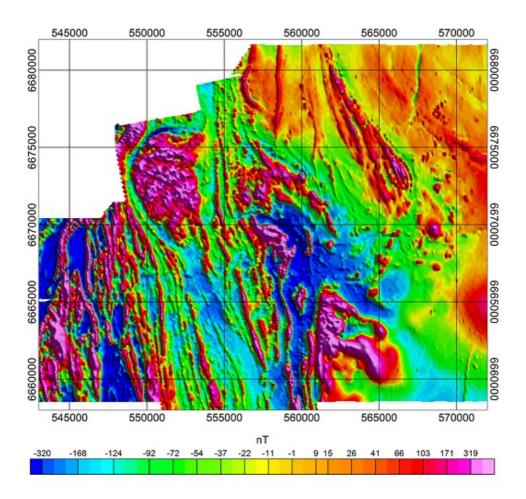


Figure 3.5 – Merged magnetic anomaly.

3.5.3 Filters

There are two main filtering classes, *high-pass* and *low-pass* filters. The goal of these filters is to suppress or enhance the source signal. A high-pass filter will emphasize the shorter wavelengths and suppress longer

wavelengths while a low-pass filter will do the opposite. Since wavelengths are associated with source depth they are useful to establish a rough depth estimate. Typically short wavelengths always originate from shallow sources, these wavelengths will be emphasized by a high-pass filter. Longer wavelength typically originates from deep sources or large shallow sources. these wavelengths will be emphasized by a low-pass filter. This is explained in Figure 3.6. This chapter focuses on different types of high-pass filters and their ability to enhance structural features like shear zones.

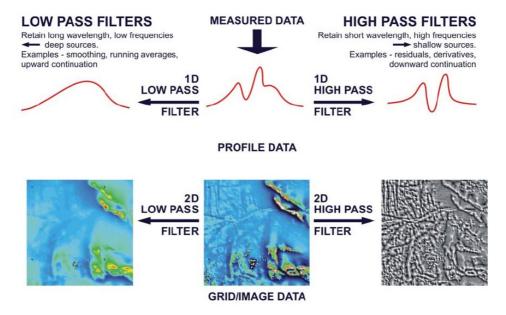


Figure 3.6 – Summary of the mechanics of filtering (Isles and Rankin, 2013).

Vertical derivative

The first order derivative (1VD) is the vertical gradient of the source signal. It is derived from the horizontal components, and it shows the change in field intensity in the vertical direction. An easy way to visualize this is given by Figure 3.7. This example shows field intensity at two heights and the difference between them gives the vertical gradient $\delta H/\delta z$. Since the maximum difference occurs at the anomaly (or TMI) peak, it will more closely reflect the lateral size of the source. In general

the 1VD is positive over the anomaly source, is zero over the edges and negative outside the source.

The second vertical derivative (2VD) can also be calculated by further derivation of 1VD, producing an even narrower anomaly. It enhances, in greater detail than 1VD, the high-frequency parts of the anomaly. However this also enhances the high-frequency noise, and unless the dataset is of very high quality it will be more difficult to separate noise from source signal. So even if the second derivative reflects the form of the signal source better, the 1VD could produce a cleaner image of easier and geologically meaningful interpretation.

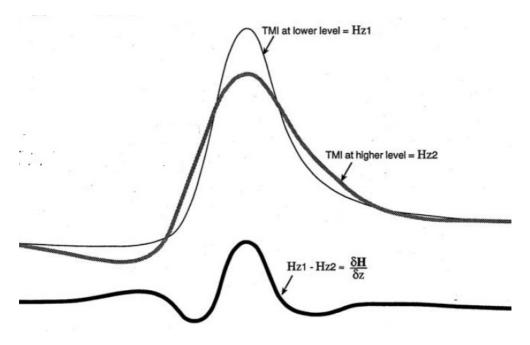


Figure 3.7 – First vertical derivative visualized. The 1VD, $\delta H/\delta z$, is the difference between the magnetic anomaly at two different heights (Hz1 minus Hz2).

Total Horizontal Derivative

The total horizontal derivative (THDR) is the most basic edge detector of the source signal. It is the combination of the two horizontal directions and is given by the following equation

$$THDR = \frac{\delta F}{\delta h} = \sqrt{\left(\frac{\delta F}{\delta x}\right)^2 + \left(\frac{\delta F}{\delta y}\right)^2} \tag{3.1}$$

Due to the nature of the mathematical equation it will always be positive and it will peak over the source edges and zero on top of the source.

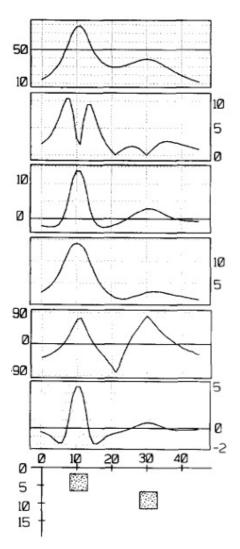
Tilt Derivative

Both 1VD and THDR will produce good results when the number of signal sources is low. When multiple sources at varying depth create interfering signals these methods will often fail to produce a satisfying image. Deeper sources suffer more, and may get completely lost.

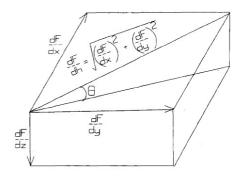
The tilt derivative (TDR) overcomes this problem by normalizing the depth of the source. This is done by dealing with the ratio of the vertical derivative and the total horizontal derivative. It is given by the equation

$$TDR = \theta = \tan^{-1} \left(\frac{1VD}{THDR} \right) \tag{3.2}$$

When dealing with the ratio of the vertical and horizontal derivative, both will be smaller for deeper sources. Thus the ratio will be large over the anomaly, pass through zero close to the edge and negative outside the source. This goes for both deeper and shallow sources. By expressing the ratio as an angle it will always be limited between $-(\pi/2)$ and $\pi/2$. Figure 3.8b explains the geometry of the tilt angle and how it will be negative when 1VD is negative, ie outside the source, zero when 1VD is zero and horizontal is maximum, and positive when 1VD is at maximum and THDR is at minimum.



(a)Different potential field measures produced by two blocks at different depth. From top to bottom: gravity anomaly in mGal, horizontal derivative in mGal/km, first vertical derivative in mGal/km, analytic signal in mGal/km, tilt angle in degrees, second vertical derivativein $mGal/km^2$ (Miller and Singh, 1994).



(b) Tilt angle defined by geometric figures. Geometry used in defining the tilt Angle. df/dx = derivative of the field in the x-direction, df/dy = derivative in the ydirection, df/dz = derivative in the z-direction, df/dh =horizontalgradient of the field. Tilt angle, θ , is measured relative to the horizontal (Miller and Singh, 1994).

Chapter 4

Results

4.1 Map description and petrography

The map produced in this thesis is based on my own field work, magnetometry and previous maps produced by Johannesen (1974), Figure 2.5 and Zwaan and Larsen (2003). It is worth mentioning that Zwaan and Larsen (2003) is based on Johannesen (1974) in the area of interest. By integrating these three studies with my own observations, I have produced an updated map of the Væleren - Sarasåsen area shown in Figure 4.1. It is also available in Appendix B.1 in a bigger format. By having the advantage of the use of digital mapping and geophysical data I was able to map the Sarasåsen intrusion more precisely.

In the following, a short description of the main lithologies is provided.

4.1.1 Meta-arkose

Meta-arkoses are one of the main lithologies in the area. They are found along the entire eastern side of the mapped area (Figure 4.1). To the west they pass to the dioritic gneisses. They also host several intrusions including the Sarasåsen Intrusion and several meta-gabbroic bodies. They contain several layers of biotite rich horizons, which are interpreted to be shales deposited in the same sequence as the hosting arkose. Metaarkoses have a persuasive regional foliation oriented N-S.

In hand specimen they consist mainly of equigranular feldspar and

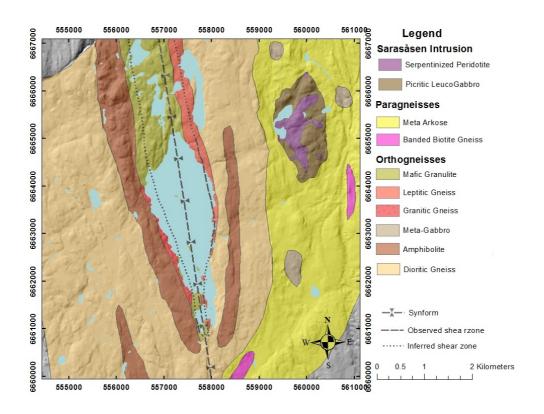


Figure 4.1 – Lithologic map produced by this study. Coordinate grid is UTM32N.

quartz. They contain minor amounts of evenly distributed muscovite and locally high amounts of biotite. Where biotite is predominant, the rock was mapped as *banded biotite gneiss*. Feldspars include both plagioclase and K-feldspar. The color of the rock varies.

In thin section (Figure 4.2a and 4.2b) the rockhas a equigranular structure with average grain size between 0.5 and 2 mm. The composition is given by quartz, plagioclase, biotite, muscovite, oxides and minor garnet.

Quartz shows undulose extinction in some grains. Grain boundaries are often decorated by oxides. The same oxides often act as pinning structure to impede crystal growth.

Plagioclase is anhedral and is usually dusty in appearance. Albite twins are sometimes visible. Boundaries to quartz are often defined by a thin sliver of oxide, but not boundaries between other plagioclase grains.

Biotite is evenly distributed throughout the studied meta-arkoses. There is a clear consistent orientation of the grains.

Garnet is not abundant and when found it is subhedral to euhedral crystal shape.

4.1.2 Banded Biotite Gneiss

The mapped banded biotite gneiss is part of the meta-arkosic sequence described above. It is differentiated because of its high biotite content. The dominant mineral assemblage is quartz, plagioclase, biotite and muscovite. The rock also contains a small amount of garnet and cordierite. The high biotite content is indeed a diagnostic feature especially at the outcrop and in hand specimens. In thin section (Figure 4.2e and 4.2f) the biotite shows a clear preferred orientation which imparts the rock a very clear foliation.

Quartz is an hedral, fine grained and characterised by undulose extinction in some of the larger grains.

Plagioclase is anhedral and fine grained. It contains albite twins and is dusty in appearance due to sericitization.

Biotite is abundant with individual crystals up to 4 mm in size.

Muscovite is modally subordinate to biotite. The grains are large, up to cm scale and do not always align with the main orientation of biotite.

Only a few grains of *Cordierite* were observed in thin section. It has a discrete twinning and is altered to chlorite and muscovite along cracks. Its presence suggests high-grade metamorphism.

Garnet is sub- to euhedral. Grains are around 3-4 mm.

4.1.3 Mafic granulite

Mafic granulites are enclosed between the two flanks of the large scale fold shown on the field map (Figure B.1). In the east they border the leptitic gneiss and in the west it borders the granitic gneiss and amphibolite.

The rock is extremely fine grained with the consequence that in hand specimen it appears almost entirely black. Granulites are generally massive, with little or no visible foliation. They are composed by pyroxenes, amphibole, plagioclase and biotite. In thin section (Figure 4.3c and 4.3d) the rock is fine grained and equigranular, except for the plagioclase which is coarser with a size up to 1 mm. It is anhedral and variably altered. Some grains are heavily sericitized while others appear completely fresh and show sharp albite twinning.

Amphibole is anhedral and is evenly distributed throughout rock mass. Some of the amphiboles appear to be retrograde, forming retrogression products of primary clinopyroxenes.

Clinopyroxene and orthopyroxene are often observed as forming aggregates with amphibole. There seems to be evidence of both prograde granulite metamorphism with amphiboles passing to pyroxene, but also retrograde amphibolite alteration.

Biotite There are two generations of biotite, characterised by greenish and brownish colours, respectively. There is no preferred orientation in the biotite grains.

4.1.4 Leptitic Gneiss

Leptitic gneisses are located along the eastern side of Lake Væleren and are sandwiched between dioritic gneisses in the east and mafic granulites in the west (Figure 4.1). They are the main lithology affected by the Væleren Shear Zone, as described later in this chapter.

In hand specimen the rock is very leucocratic. It is very fine grained with with almost no visible mafic minerals. There is also an augenstructure defined by K-feldspar. There is a weak foliation that is more visible when mafic bands are present.

Thin sections (Figure 4.4e) show the same structures as in hand specimens. There are large K-feldspar augens, around 3 mm in size. The rest of the mineral assemblage is between <0.1 mm up to 0.2 mm size. This assemblage is quartz, plagioclase, K-feldspar, garnet and amphibole.

Quartz shows undulose extinction. Grain boundaries are rounded.

 $Plagioclase\ {\rm still}\ {\rm show}\ {\rm weak}\ {\rm albite}\ {\rm twinning}.$ Most grains are sericitized.

K-feldspar occurs both as very fine grained, and as large augen-like structures. The augens also have corona-like structures consisting of medium sized K-feldspar grains.

Garnet is sub- to anhedral. It is fine grained and scarce.

4.1.5 Granitic Gneiss

Granitic gneisses are located along most part of the eastern shore of Lake Væleren (Figure 4.1). They are found between amphibolites to the east and mafic granulites in the west. Hand specimens show a porphyritic structure, medium to coarse grain size except for porphyritic K-feldspar. However, the grainsize seems to vary from samples from western side of Lake Vælerens being coarser to the samples from the eastern side. The rock also has a penetrative foliation defined by the orientation of biotite and stretched quartz grains.

In thin section (Figure 4.3a and 4.3b) the rock is porphyritic with a mineral assemblage containing of K-feldspar, plagioclase, quartz, biotite and chlorite. It also contains very small amounts of amphibole. Chlorite is not observed in the gneiss from the eastern side of the lake, while samples from western side of Væleren contain both biotite and chlorite.

K-feldspar ranges from coarse grained, cm-scale to medium sized anhedral grains. It shows tartan twinning and oriented fractures.

Plagioclase is anhedral medium grained with albite twins. It is clouded and partly sericitized. It does not show the same fracturing as the k-feldspar.

Quartz also varies in grain size and shows undulose extinction. It does not show the fracturing of the feldspars but it does show an orientation of inclusions, suggesting possible annealing of previously existing fractures.

Biotite is fine grained and partly altered to biotite. It is oriented, defining the foliation of the rock.

Chlorite is fine grained and oriented the same way biotite is.

4.1.6 Meta-gabbro

The rock is equigranular and medium grained, with a tendency for the felsic minerals to be slightly larger than the mafic phases. The rock consists of plagioclase, pyroxene, amphibole and oxides. The metagabbros in the area are generally pervasively foliated in hand specimen, with the foliation defined by preferred grain orientation. Pyroxene has a symplectitic amphibole/plagioclase corona that ranges from less than 1 mm in thickness to a complete replacement of pyroxene (Figure 4.2c).

Plagioclase is present in laths with no preferred orientation. It has strong albite twinning. Plagioclase is also present as fine grained symplectite together with amphibole in pyroxene coronas.

Clinopyroxene is primary but is partly or sometimes completely altered to amphibole, an alteration that starts at the edges of the grains and gradually propagates to the entire grain. There are intragrain fractures with a preferred orientation and fracturing also affects altered amphibole coronas.

Garnet is present in very low amount, though some grains can be up to 5 mm in diameter. It is generally anhedral and it is observed to mostly grow along the edges of other grains.

4.1.7 Amphibolite

Amphibolites can be seen on Figure 4.1 as elongated bodies stretching in N-S direction. They occurs within dioritic gneisses as more mafic interpreted intrusives. In hand specimen the rock is medium grained. It has equigranular texture except for garnets which can be coarser.

Investigation of thin sections (Figure 4.3e and 4.3f) reveals two different compositions as a function of where, with respect to Lake Væleren, the amphibolite was collected. Amphibolites from the western side contain garnets, is instead absent in samples from the eastern side. But the western side lacks biotite and the eastern side is fairly rich in it. Otherwise the mineral composition is predominately plagioclase and amphibole. The eastern side also has a clear orientated structure. This is very well reflected in oriented biotite.

Plagioclase is anhedral and medium grained. It is altered in most cases but it still shows albite twinning.

Amphibole is anhedral to subhedral medium grained. Amphiboles show signs of being altered to biotite.

Biotite is medium to fine grained. Its orientation helps define the foliation of the rock.

Garnet are subhedral to euhedral medium to coarse grained. Samples are rich in garnets locally.

4.1.8 Dioritic gneiss

Dioritic gneisses are one of the dominant lithologies in the mapped area together with the meta-arkoses. They dominate the western part of the mapped area, and also a large part of the eastern side of Væleren as seen on the map (Figure 4.1).

In hand specimen the rock is medium to fine grained and leucocratic. It has some mafic minerals but is dominated by felsic phases. There are some outcrops that show distinct banding consisting of felsic and mafic bands, creating a very pervasive foliation.

In thin section (Sample BLA-1) the same banding is visible and the foliation is given by the shape of grains in addition to a compositional banding. The texture is porphyritic with large plagioclase grains. The mineral assemblage is amphibole, pyroxene, plagioclase, quartz and garnet.

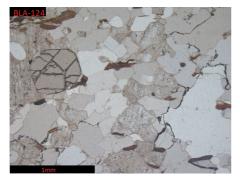
Amphibole is fine grained. It is partly altered to pyroxene.

Pyroxene is located in bands parallel to the foliation of the rock.

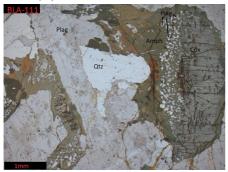
Plagioclase is present both as porphyritic and small grained. The larger grains show albite twinning and is partly sericitized, as is the smaller grains.

Quartz is fine grained. Some grains show undulose extinction. This suggest recrystallization of quartz since some grains do not show extinction.

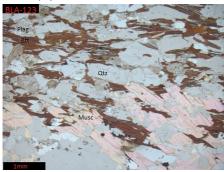
Garnet is present in bands, much the same way as pyroxene. They are an hedral to subhedral.



(a) Plane polarized light



(c) Plane polarized light



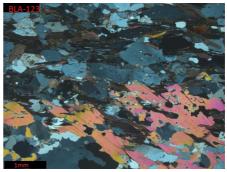
(e) Plane polarized light



(b) Cross polarized light

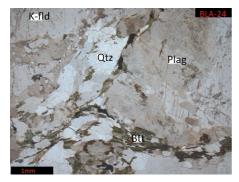


(d) Cross polarized light.

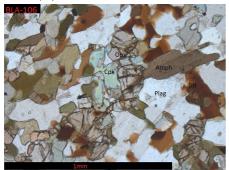


(f) Cross polarized light.

Figure 4.2 – Plate with thin section micro-photos. (a) and (b): Meta-arkosic samples, (c) and (d): Meta-gabbros (e) and (f): banded biotite gneiss. See Table A.1 for location of samples.



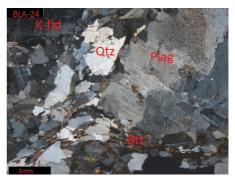
(a) Plane polarized light



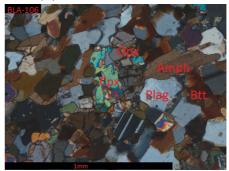
(c) Plane polarized light



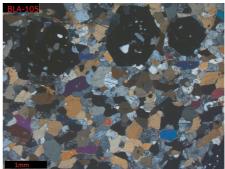
(e) Plane polarized light



(b) Cross polarized light

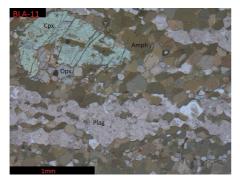


(d) Cross polarized light.

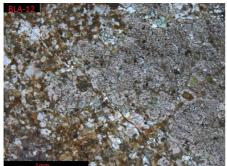


(f) Cross polarized light.

Figure 4.3 – Plate with thin section micro-photos. (a) and (b): Granitic gneiss, (c) and (d): Mafic granulite, (e) and (f): Amphibolites. See Table A.1 for location of samples.



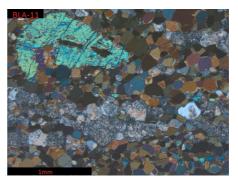
(a) Plane polarized light



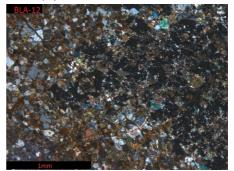
(c) Plane polarized light



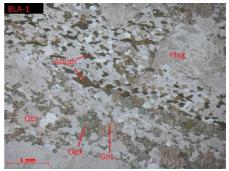
(e) Cross polarized light



(b) Cross polarized light



(d) Cross polarized light.



(f) Plane polarized light.

Figure 4.4 – Plate with thin section micro-photos. (a) and (b): First generation dike, (c) and (d): Second generation dike. (e): Leptitic gneisses and (f): Dioritic gneisses. See Table A.1 for location of samples.

4.2 Petrographic investigation and mineral chemistry of the Sarasåsen intrusion

The Sarasåsen intrusion consists of a leucogabbro body which contains layers of serpentinized peridotites, see map (Figure B.1. In order to investigate whether the ultra mafic body was a part of an ophiolite complex trapped in a suture zone or a cumulate in a magma chamber, selected samples was analysed in an electron probe microanalyser. The intrusion is hosted in meta arkoses. Xenoliths of foliated banded gneiss are found within the intrusion. Two outcrops with large meter scale xenoliths are found (UTM32N 560104-6665254 and 559728-6665261) dipping 57/204 and 80/050 respectively. The leucogabbro has a characteristic light purple color that originates from the plagioclase. It consists mainly of plagioclase and interstitial clinopyroxene. However some outcrops also reveal a picritic gabbro with partly serpentinized olivine. The olivine is sorrounded by double coronas in contact with the plagioclase. The innermost corona consists of orthopyroxene and, if present, the second is a symplectite of spinel and clinopyroxene. The peridotite is heavily serpentinized. There is almost no olivine left. The heavily serpintinized olivines have the same coronas as the olivine in the leucogabbro. Samples from the Sarasåsen intrusion were analysed in a microprobe and the following section will present the results together with a petrographic description. Tables B.1, B.2, B.3, B.4, B.5, B.6, B.7, B.8, B.9 and B.10 show all reduced data.

4.2.1 Leucogabbro

Igneous assemblage

All samples contain mainly igneous minerals with olivine, plagioclase and clinopyroxene being the main phases. Olivine and plagioclase occur as the cumulus phase and clinopyroxene intercumulus. The leucogabbro is massive and equigranular and has a subophitic texture with plagioclase partially enclosed in clinopyroxenes.

Olivine occurs as rounded grains with an inner corona of orthopyroxene and a second corona being a symplectite of spinel and amphibole or clinopyroxene. The olivine is partly serpentinised and some grains are altered to talc as in Figure 4.5c where the entire grain appears pseudomorphic after replaced olivine. The chemistry analysis of the olivine did not reveal any zoning and the composition is very homogeneous within grains and across all samples (Table B.1-B.6). Composition ranges from Fo_{82} to Fo_{84} .

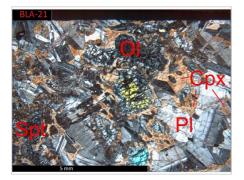
Plagioclase laths are subhedral to euhedral and show albite, pericline and Karlsbad contact twinning (Figure 4.5e). The plagioclase grains surrounding serpentinized olivine show distinct radial fractures centered on the olivine grains. Plagioclase composition is more heterogeneous than that of olivine, suggesting a zoning. It ranges from An_{80} to An_{95} .

Clinopyroxene is an hedral and occurs only as intercumulus between plagioclase and olivine. It has a homogeneous diopside composition of $En_{44-46}Fe_{4-6}Wo_{48-50}$.

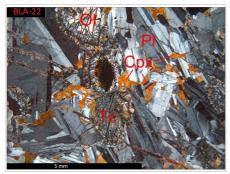
Secondary alteration

The olivines show one or two sets of coronas. The inner corona, consisting of orthopyroxene, is always present (Figure 4.5a, 4.5c, 4.5e). The width of the corona ranges from 50 μ m to 100 μ m. Contacts between olivine and orthopyroxene coronas are often convex towards the olivine, suggesting orthopyroxene grew at the expense of olivine (de Haas et al., 2002). The second corona, which is a symplectite consisting of spinel and amphibole

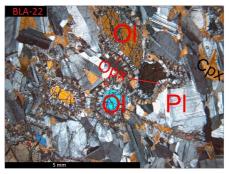
Figure 4.5 (facing page) – Plate showing (a): sample BLA-21, showing a picritic leucogabbro in crosspolarized light. It contains plagioclase, interstitial clinopyroxene and olivine with orthopyroxene coronas. Olivine is partly serpentinized in fractures. (b): Electron backscatter image from BLA-21 showing serpentinized olivine with an orthopyroxene corona, plagioclase and an interstitual clinopyroxene between opx corona and plagioclase. Plagioclase altered to pumpellyite in plagioclase hosted fractures. (c): sample BLA-22, olivine is completely altered to talc due to hydration along fractures. Note the almost unaltered olivine in upper part of image that is not connected to fractures. (d): Same sample as (b) but with clinopyroxene/spinel symplectite in upper left corner. (e): sample BLA-22, with pumpellyite in plagioclase-hosted fractures.



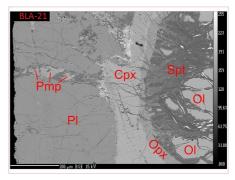
(a) Cross polarized light.



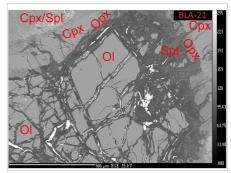
(c) Cross polarized light.



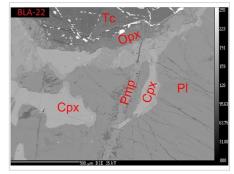
(e) Cross polarized light.



(b) Electron backscatter.



(d) Electron backscatter.



(f) Electron backscatter.

or clinopyroxene (the symplectite is so fine grained that a good sample was hard to obtain) is only present in contact with plagioclase. The composition of the orthopyroxene coronas is quite homogeneous ranging between $En_{82-83}Fs_{16-17}Wo_{0-1}$. The olivine itself is all serpentinized to a varying degree. The serpentine alteration seems to be fluid driven and contains varying amounts of Al. This suggests lizardite type serpentine. Figure 4.5e show the least serpentinized olivine where only small fractures are serpentinized. Figure 4.5a shows an example of olivine in the same sample with more fractures and thus more pervasive serpentinization. This is also reflected in the plagioclase where pumpellyite is crystallized along fractures. Figure 4.5c shows an olivine grain cut by a large fracture and the grain is completely altered to talc in this case.

Plagioclase and pyroxene seem mostly unaltered. The plagioclase is altered to pumpellyite along fractures due to fluid flow.

4.2.2 Serpentinized Peridotite

The peridotite contains mostly metamorphic minerals. It is much more altered than the neighbouring leucogabbro. The mineral assemblage is given by now serpentinized cumulus olivine and intercumulus clinopyroxene and altered plagioclase. There is also a pervasive layering in the intrusion in certain outcrops but no consistent orientation throughout the intrusion has been recorded. However the majority of the layering seem to dip gently to the south west.

Igneous assemblage

Olivine is rounded and it is nearly completely replaced by pseudomorphic serpentine (Figure 4.6a and 4.6e). It has the same coronas as the olivines in the leucogabbro although the second symplectitic corona is rare due to limited availability of plagioclase. The composition of the olivine is homogeneous and very much like the olivine of the leucogabbro. It ranges from Fo_{83} to Fo_{85} .

Plagioclase is anhedral intercumulus and is in most cases completely altered to carbonate or a hydrous phase like pumpellyite or prehnite. However some grains still preserve igneous textures and still visible albite twins (Figure 4.6c. The composition of analysed plagioclase is An_{85} to $\mathrm{An}_{87}.$

Clinopyroxene is anhedral and occurs as intercumulus between olivine. Orthopyroxene sometimes occurs as exsolution in the clinopyroxene. The composition of the intercumulus clinopyroxene is $En_{46}Fs_6Wo_{48}$, making it a diopside.

Spinel. A few grains of brown euhedral magnesiochromite is present in sample BLA-19 (Figure 4.6a and 4.6b). It contains 28 wt% Cr₂O₃.

Ilmenite. Anhedral ilmenite grains sometimes appear as intercumulates together with clinopyroxene.

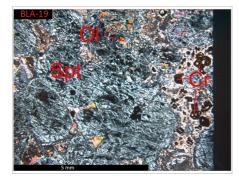
Secondary alteration

Olivine coronas are much like the coronas found in the leucogabbro. There are two sets of coronas. The innermost consists of orthopyroxene and is between 50μ m and 100μ m thick. The composition of the orthopyroxene is very homogeneous and is $En_{82-83}Fs_{16-17}Wo_{0-1}$. The second symplectite corona of spinel and clinopyroxene or amphibole occur less. This is because it only exist in contact between olivine and plagioclase and the rock is poor in plagioclase.

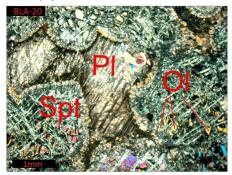
Alteration of olivine. The olivine is almost completely serpentinized as seen in Figure 4.6a, 4.6c and 4.6e. The serpentine are pseudomorphic as the original olivine shape is reflected in the serpentine. There seems to be a fluid driven alteration, and together with the relatively high content of Al this suggest lizardite type of serpentine.

Alteration of pyroxene. The clinopyroxene is mostly unaltered. However exsolution of orthopyroxene is present in some grains. The orthopyroxene in the olivine coronas is also locally serpentinized together with the olivine. This is evidence that serpentinization post-dates corona formation.

Alteration of plagioclase. The plagioclase is almost completely altered in most samples. However as seen in Figure 4.6c there are still visible primary structures in the plagioclase grain. But usually the plagioclase is altered to prehnite and pumpellyite. Figure 4.6 (facing page) – Plate with micro-photographs (a) Sample BLA-19: almost completely serpentinized olivine with orthopyroxene coronas, intercumulus clinopyroxene and spinel. (b) Sample BLA-19: Serpentinized olivine with orthopyroxene coronas which are also partly serpentinized. Magnesiochromite is also present. (c) Sample BLA-20: Intercumulus plagioclase partly altered to prehnite and possibly other hydrous phases. The plagioclase crystallized between cumulus olivine that is now almost completely replaced by pseudomorphic serpentine. (d) Sample BLA-14: Serpentinized olivine with coronas of orthopyroxene. Symplectite of clinopyroxene and spinel between olivine grains. A mm scale ilmenite grain is also visible. (e) sample BLA-20: Serpentinized olivine with orthopyroxene coronas and interstitial clinopyroxene. (f) sample BLA-20: Serpentinized olivine with large interstitial clinopyroxene.



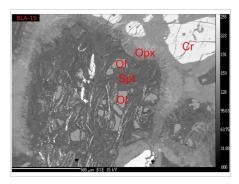
(a) Cross polarized light.



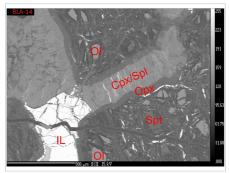
(c) Cross polarized light.



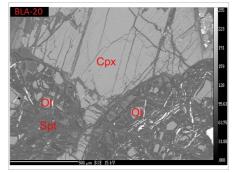
(e) Cross polarized light.



(b) Electron backscatter.



(d) Electron backscatter.



(f) Electron backscatter.

4.2.3 Petrology of Sarasåsen intrusion

From calculated cations in tables B.1, B.2, B.3, B.4, B.5 and B.6 end members of olivine, pyroxenes and plagioclase were calculated and are presented in Table 4.1. The end members are plotted in Figure 4.7 which includes both analysis from the leucogabbro and the serpentinized peridotite. All plotted end members are derived from the primary igneous assemblage. A very homogeneous composition is seen in pyroxenes and olivines. Plagioclase shows more spread in composition but this could be due to zoning. This is unconfirmed as no strategy with regard to where on the mineral analysis was done. But the homogeneous composition in olivine and pyroxenes suggests all analysed minerals are crystallized from the same magma composition.

pyroxenes.	2
and	
clase	
iio	
pla_{0}	-
of olivine.	
of ol	
<i>d</i> members	
end	
showing	
Table	
1.1	
4	
Table	

Sample	Point	Mineral	End member
	55/1	Olivine	Fo _{82.8} - Fa _{17.2}
	57/1	Olivine	Fo _{83.3} - Fa _{16.7}
	68/1	Olivine	Fo _{83.4} - Fa _{16.6}
	69/1	Olivine	Fo ₈₄ - Fa ₁₆
BLA-13	60/1	Plagioclase	$Ab_{20.2} - An_{79.7} - Or_{0.1}$
	61/1	Plagioclase	Ab _{18.8} - An _{81.8} - Or _{0.1}
	75/1	Plagioclase	$Ab_{15.3} - An_{84.6} - Or_{0.1}$
	58/1	Orthopyroxene	Eng2.3 - Fs _{15.8} - Wo _{1.9}
	72/1	Orthopyroxene	En84.1 - Fs _{15.5} - Wo _{0.4}
	115/1	Olivine	Fo83.6 - Fa _{16.4}
	116/1	Olivine	F083.5 - Fa _{16.5}
BLA-14	1/2	Olivine	Fo _{83.5} - Fa _{16.5}
	9/2	Olivine	Fo _{83.5} - Fa _{16.5}
	119/1	Orthopyroxene	En84.2 - Fs _{15.3} - Wo _{0.5}
BLA-15	111/1	Plagioclase	$Ab_{5.3}$ - $An_{94.6}$ - $Or_{0.1}$
BLA 16	97/1	Clinopyroxene	En46.3 - Fs4.5 - Wo49.2
	105/1	Clinopyroxene	En44.9 - Fs _{6.4} - Wo _{48.7}
	76/1	Olivine	F082.5 - Fa _{17.5}
	77/1	Olivine	F082.5 - Fa _{17.5}
	81/1	Olivine	Fos2.5 - Fa _{17.5}
BLA-17	82/1	Olivine	Fo _{82.4} - Fa _{17.6}
	80/1	Orthopyroxene	Ens3.6 - Fs _{16.1} - Wo _{0.3}
	85/1	Orthopyroxene	En83.6 - Fs15.9 - Wo _{0.5}
	89/1	Plagioclase	$Ab_{13.3} - An_{86.7} - Or_0$

I Galanan	plagroci	owvme, puagrociase ana pyroxenes.	enes.
Sample	Point	Mineral	End member
DI A 10	23/2	Olivine	Fo _{84.7} - Fa _{15.3}
01-970	31/2	Olivine	$Fo_{84} - Fa_{16}$
DI A 10	32/2	Olivine	Fos2.6 - Fa17.4
AT-MULU	34/2	Orthopyroxene	En83.4 - Fs _{16.2} - Wo _{0.4}
	15/2	Olivine	Fos2.9 - Fa _{17.1}
	16/2	Olivine	F082.5 - Fa17.5
DI A 90	19/2	Olivine	Fos3 - Fa ₁₇
07-WTG	20/2	Olivine	Fo ₈₃ - Fa ₁₇
	18/2	Orthopyroxene	En83.4 - Fs _{16.1} - Wo _{0.5}
	22/2	Clinopyroxene	En46.3 - Fs5.8 - Wo49.9
	1/1	Olivine	Fos2.1 - Fa _{17.9}
	2/1	Olivine	Fo _{81.7} - Fa _{18.3}
	17/1	Olivine	Fo81.6 - Fa18.4
BLA-21	18/1	Olivine	Fo _{81.7} - Fa _{18.3}
	4/1	Orthopyroxene	Ens2.8 - Fs16.8 - Wo _{0.4}
	12/1	Plagioclase	Ab _{17.5} - An _{82.4} - Or _{0.1}
	13/1	Plagioclase	Ab _{19.3} - An _{80.6} - Or _{0.1}
	34/1	Olivine	Fos2.6 - Fa _{17.4}
	39/1	Olivine	Fos2.1 - Fa _{17.9}
	40/1	Olivine	Fos2.2 - Fa _{17.8}
RI.4-99	22/1	Clinopyroxene	En44.5 - Fs6.0 - Wo49.5
77-WILL	24/1	Orthopyroxene	Ens3.3 - Fs _{16.3} - Wo _{0.4}
	43/1	Clinopyroxene	En44.2 - Fs6.3 - Wo49.5
	44/1	Plagioclase	Ab _{16.7} - An _{83.2} - Or _{0.1}
	45/1	Plagioclase	Ab _{17.5} - An _{82.4} - Or _{0.1}

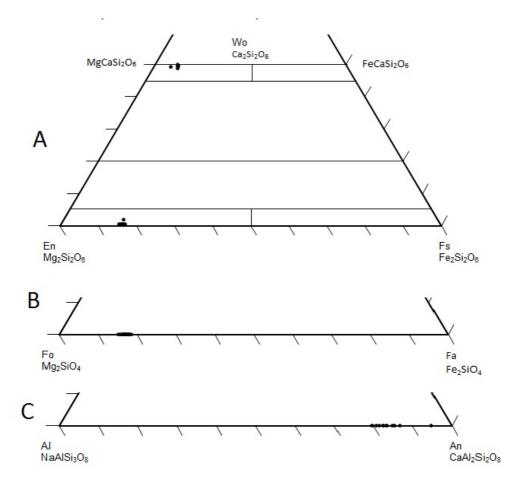


Figure 4.7 – End members calculated from microprobe analysis from the Sarasåsen intrusion. Only primary igneous phases are included. Samples are taken from both the leucogabbro and the serpentinized peridotite. (A) Clino-and orthopyroxene indicating diopside and enstatite composition. (B) Olivine with a homogeneous $Fo_{(82-84)}$ composition. (C) Plagioclase composition.

4.3 Structural framework of the area: a synopsis

The mapped area is characterised by a relatively simple first order structural template. As shown by the map (Figure B.1) the main regional foliation trends about NS and shows only minor variations. There is some dispersion about this mean trend, which I interpret as mostly due to the tight to isoclinal folds (see below) that deform the exposed lithologies and the presence of more competent mafic clasts within the foliation that cause local deflections of the planar fabric. The foliation is concordant with the main lithological boundaries and the most significant magnetic anomalies, which indeed define the local N-S to NNW-SSE trending structural grain.

Mapping revealed the existence of an hitherto unreported spectacular shear zone, which is named herein the Væleren Shear Zone (VSZ), from the name of the lake in the middle of the mapped area, along whose coastlines it is most spectacularly exposed.

The VSZ is defined by a strongly sheared belt, up to several meters thick, that, similarly to the regional foliation in its hanging wall and footwall, trends NS, although with some dispersion about this direction. The shear fabric is defined by mylonitic to ultramylonitic amphibolite-facies leptitic gneisses and fine grained metavolcanic sequences of intermediated composition. The leptitic gneiss is interpreted as the result of pervasive ductile shearing of a granitic gneiss protolith that can be found adjacent to the shear zone in domains of lower finite strain. Strain can be rather heterogeneously distributed, with ultramylonitic bands separated by significantly lower strain volumes. Structural mapping shows that the mylonitic foliation along the eastern shoreline of Lake Væleren bears a mean stretching lineation oriented N-S (Figure 4.9a and 4.9b). The stretching lineation can be very pervasive and is defined by strongly elongated quartz along the foliation surfaces. Mylonites ascribed to the VSZ along the western shore of the lake, however, bear a differently oriented stretching lineation. As shown by stereonet of Figure 4.9c, lineations there plunge with a mean plunge of 08° toward 343° .

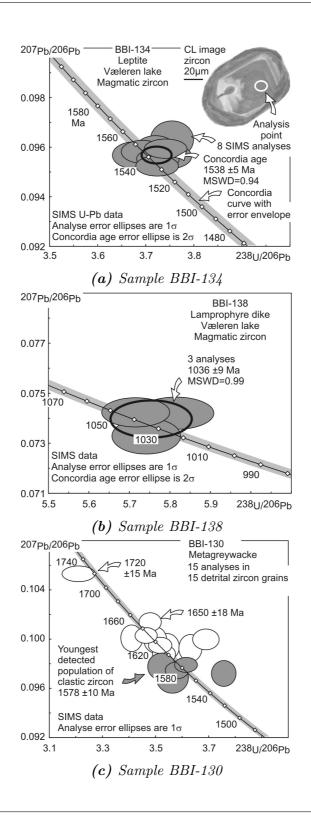
The kinematics of the VSZ is unravelled by numerous kinematic in-

dicators found in association with the penetrative stretching lineation. Sinistral and dextral sense of shear were documented on the eastern and western coast line, respectively. The different kinematic framework, although initially thought to be possibly due to two separate shearing events of different age, is now interpreted as reflecting the result of large scale tight to isoclinal folding affecting the entire shear zone about a steeply NW-plunging fold axis. Within the VSZ mylonitic package, two generations of mafic dikes folded isoclinally around subvertical axes are transposed parallel to the mylonitic foliation. In addition, a later EWstriking and thus discordant lamproitic dyke helps to add constraints to the ductile deformational history of the region. (Figure 4.10) The latter was dated by Dr. Bingen from the NGU to ca. 1036 Ma. This age constraints all ductile deformation in this area to pre 1036 Ma (Figure 4.8b).

4.4 U-Pb Geochronology

SAMPLE BBI134 is a fine-grained felsic gneiss, representing the leptite body in the Væleren shear zone (UTM 32v 558047-6663014). The sample is collected along the shore of lake Væleren. The felsic gneiss dominates the outcrop and it is interlayered with thin layers of mafic gneiss (first generation of dykes). The outcrop shows a strong planar fabric. The samples contains biotite (green and largely altered to chlorite), amphibole, epidote and an opaque mineral, in a fined grained quartzofeldspathic matrix (<100 μ m). It contains rounded to prismatic zircon, 100-150 μ m in size, with rounded tips. Cathodoluminescence images of the zircon reveal an oscillatory zoning, indicating growth in magmatic conditions (see CL image in Figure 4.8a). Eleven U-Pb analyses were performed in 11 zircon crystals. Three of them are widely discordant and discarded for interpretation. The 8 remaining analyses are concordant (i.e. they

Figure 4.8 (facing page) – Concordia diagrams showing geochronology results of (a): leptitic gneiss west of Lake Væleren, (b): lamprophyre dike cutting the Væleren Shear Zone and (c): Meta-arkose hosting Sarasåsen intrusion. Figures produced by B. Bingen.



are overlapping the concordia curve at the 2 sigma uncertainty level) and are overlapping each others. Therefore these 8 points allow to calculate a concordia age, as defined by Ludwig (1998) (i.e. the concordia age is the shortest projection of the centroid of the data cluster onto the concordia curve). The calculated concordia age is 1538 ± 5 Ma, and it records magmatic crystallization of the zircon (Figure 4.8a). By inference, it also records the magmatic crystallization of the protolith of the gneiss. The good clustering of the data is a good indication that the protolith of the gneiss is a magmatic rock, probably a plutonic rock. The age of 1538 Ma is equivalent to the age of several orthogneiss samples in the northern and eastern part of the Kongsberg terrane. It indicates that the protolith onto which the shear zone developed is the dominant regional orthogneiss of Gothian age. It also provides a maximum age for the shearing event. The CL images and the U-Pb data do not show any evidence for neoformation of zircon rims or episodic Pb loss from the zircon during the Sveconorwegian orogenic event. Zircon crystals have a typical grain-size (100-150 μ m) for a felsic plutonic rocks, and, except for the fact that they are rounded, they do not seem to have been affected by the shearing event observed in the outcrop. The typical grain size of zircon contrasts with the small grain size of the quartzofeldspathic matrix. This contrast suggests that the fine-grained nature of the matrix is the result of mylonitic grain-size reduction. This supports the interpretation that the leptite is a mylonitic rock.

SAMPLE BBI138 is taken ca. 100 m away from sample BBI134, in the weakly deformed central part of an E-W trending lamprophyre dyke along lake Væleren (UTM 32v 558049-6663115). This dyke sharply crosscuttes the mylonitic fabric with an angle of 70° and therefore intrusion of the dyke postdates the main deformation event observed in the outcrop. The whole-rock contains close to 600 ppm Zr (as determined by XRF, Table 4.2) and the sample provided abundant large prismatic zircon crystals, up to 400 μ m in length. However, zircon is rich in U and Th (>1000 ppm) and almost all crystals are dark brown to black and highly metamict. Only a few partly transparent crystals could be recovered. Six U-Pb analyses were performed in two sector zoned crystals, and only three of these are concordant in the concordia diagram. These three analyses are statistically equivalents and therefore yield a concordia age of 1036 ± 9 Ma (Figure 4.8b). This age records magmatic crystallization of the zircon and magmatic crystallization of the dyke. The age of 1036 Ma is a key regional time marker, as it provides a minimum age of ca. 1036 Ma for the deformation in the outcrop. The data on the leptite (sample BBI134) and the lamprophyre dyke (BBI138) bracket the deformation between ca. 1538 and 1036 Ma. These data imply that the deformation leading to the regional scale N-S trending foliation and to the N-S trending mylonitization associated with the Væleren shear zone are part of the early-Sveconorwegian Arendal orogenic phase (1140-1080 Ma) or alternatively are part of a pre-Sveconorwegian, i.e. Gothian, orogenic

Table 4.2 – Tables showing (a): major elements and (b): trace elements from XRF wholerock analysis of samples BBI 138 and BBI 139.

			Trace Elements				
				BBI 138	BBI 139		
			Sc (PPM)	29	30		
			TiO2 (%)	1.274	0.869		
			V (PPM)	179	166		
			Cr (PPM)	1592	41		
			MnO (%)	0.215	0.162		
			Fe2O3 (%)	15.196	10.252		
			Co (PPM)	21	48		
			Ni (PPM)	387	102		
			Cu (PPM)	10	23		
			Zn (PPM)	75	66		
			Ga (PPM)	21	16		
			As (PPM)	11	7		
			Rb (PPM)	44	71		
Major	Elements		Sr (PPM)	226	395		
Sample	BBI 138	BBI 139	Y (PPM)	42	100		
SiO2 (%)	42.28	48.85	Zr (PPM)	592	408		
Fe2O3 (%)	15.30	10.18	Nb (PPM)	9	17		
TiO2 (%)	1.48	1.00	Mo (PPM)				
CaO (%)	9.54	11.37	Sn (PPM)				
K2O (%)	1.98	4.69	Sb (PPM)				
P2O5 (%)	2.12	2.75	Cs (PPM)	5	9		
Al2O3 (%)	10.55	8.51	Ba (PPM)	557	1588		
MgO (%)	13.97	9.55	La (PPM)	138	199		
Na2O (%)	0.00	0.05	Ce (PPM)	303	406		
MnO (%)	0.22	0.17	Pb (PPM)	6	11		
Sum (%)	97.44	97.13	Th (PPM)	16	29		
LOI (%) 850°C	5.90	2.84	U (PPM)	5	8		
(a) Mai	or Elemer	(b) Trace Elements					

(a) Major Elements

(b) Trace Elements

phase in this part of the Kongsberg terrane.

SAMPLE BBI130 is a garnet -biotite -clinopyroxene felsic to intermediate gneiss, collected in the wall of a small abandoned quarry, close to a hill called Knarten (UTM 32v 559428-6663083). The wall is trending E-W, and thus it is perpendicular to the regional foliation and allows good observation. To the east of the sample, in the quarry, the gneiss is felsic and rich in coarse garnet and biotite, and it is interpreted as a metasediment of greywacke or psammite composition. To the west of the sample, the outcrop is more mafic and includes boudins of amphibolite. In the amphibolite, several layers rich in garnet and clinopyroxene suggest that the locality was affected by incipient granulite facies metamorphism. The sample was selected for zircon geochronology, in order to date the amphibolite to granulite facies metamorphic event. However, contrary to expectations, the separated zircon crystals do not show any evidence for metamorphic rim, and therefore, did not provide any age information on metamorphism. Zircon is prismatic to rounded and typically 100 to 200 μ m long. Zircon crystals show variably planar oscillatory zoning, consistent with crystallization in a magmatic environment. Fifteen U-Pb analyses were collected in the centre of 15 zircon crystals. All analyses but one are concordant. The analyses do not define a single age cluster. Their 207Pb/206Pb age ranges between 1650 \pm 18 Ma and 1564 ± 32 Ma with one older value at 1750 ± 15 Ma (Figure 4.8c). The scatter of dates is consistent with the interpretation that the zircon grains are detrived clasts derived from a variety of sources, and therefore that the sample represents a metasediment. The five youngest analyses yield equivalent 207Pb/206Pb ages ranging from 1584 \pm 15 to 1564 \pm 32 Ma with a weighted average value of 1578 \pm 10 Ma. The age of 1578 ± 10 Ma provides a maximum age for deposition of the sediment sequence. This number is slightly older than the maximum age of 1533 \pm 16 Ma obtained for a sample of sandstone in a graded bedded sequence in the Veme complex some 10 km northwards along strike (Bingen et al. (2001), their sample N95-128). The number of analysed detrital zircons in both samples is small (<20); however, available data suggest that the two sediment packages can either be correlated or that sample BBI130 represents a lower part (older part) of the same sediment sequence.

4.4.1 Væleren shear zone

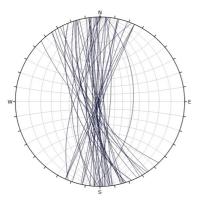
The VSZ is found along the eastern, western and southern shores of Lake Væleren (Figure B.1). It is characterised by a sub vertical N-S mylonitic foliation parallel to the regional foliation of the area investigated. As seen in Figure 4.9a the strike of the shear foliation varies by ca. 60° about the N-S direction. This is due to the fact that the shear zone hosts clasts of competent mafic lithologies such as amphibolite and metagabbro that act mechanically as rigid objects that deflect the otherwise planar shear foliation. This can be commonly observed at the outcrop (Figure 4.10d). Strain distribution within the VSZ along the eastern shore of Lake Væleren is rather heterogeneous, with bands of ultra-mylonitic textures containing convincing evidence of sinistral kinematics such as asymmetric folds and porphyroclasts (Figure 4.10). Stretching lineations related to the sinistral kinematic are shown in Figure 4.10b. They are very steep indicating dip-slip movement with only minor obliquity. The transition from the VSZ to the less deformed eastern block is rarely exposed. At one locality (Figure 4.10e), however I could map a poorly sheared gneiss containing a differently oriented, E-W striking foliation. This discordant foliation is rotated progressively into parallelism with the VSZ main trend and the geometry of the deflection indicates a component of sinistral shear along the VSZ, as confirmed by numerous other kinematic indicators (Figure 4.10e). This observation indicates the very significant transposition into the VSZ direction.

Along the southwestern side of the lake there are a few outcrops displaying interesting kinematic relationships between lower strain domains and highly mylonitic bands (Figure 4.10). The photo of Figure 4.10f, for example, shows one set of foliation planes deflected into a high strain zone oriented N-S. The deflection geometry indicates a component of dextral shearing along a stretching lineation plunging 8° toward 343. This is the same relationships described in Figure 4.10e for the eastern shore of Lake Væleren, only with opposite kinematics. This high strain mylonitic band is oriented identically in the two cases but the stretching lineations differ in their orientation (Figure 4.9b and 4.9c). This makes the two sheared foliations seemingly incompatible from a kinematic viewpoint.

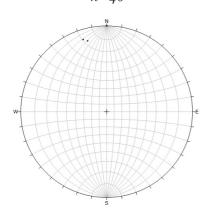
Around the southern tip of lake Væleren the regional foliation changes

orientation from N-S toward a more E-W oriented strike (Figure B.1). Folding around a steep fold axis explains this change. When plotting all foliation planes measured in the area around the southern end of the lake in a stereonet, a β -plot indicates a fold axis that plunges ca. 55/330 (Figure 4.9d). This is slightly different from the steep axes of the mesoscopic isoclinal folds that can be found throughout the shear zone (Figure 4.9e). The fold axis computed from the folding of the regional foliation can, however, be used as a rotation axis to verify if the stretching lineations from the eastern coastline (associated with sinistral kinematics) can be related to those on the western shore of the lake (associated with dextral kinematics) by folding. Due to the isoclinal nature of the folds found within the shear zone the lineations were rotated by 180° . Using stereographic projections, a mean lineation from the eastern shore was rotated around an axis plunging 60/330. The result was a very close match with the measured lineations related to dextral kinematics from the western shore (Figure 4.9). There is a difference in plunge of 5° between the applied rotation axis to the calculated β -plot, but this is well within an acceptable margin of error. I conclude therefore that the two lineation trends reflect only post-stretching/shearing folding.

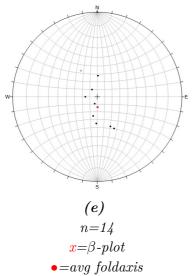
Figure 4.9 (facing page) – Stereographic projections of (a) all shearplanes related to the VSZ, (b) lineations from the VSZ associated with sinistral kinematics, (c) lineations from the VSZ associated with dextral kinematics, (d) all foliation planes from the southern part of Lake Væleren, with intersecting β -plot, (e) all fold axes measured within the VSZ plotted as black circles with an average foldaxis in red, and (f) the average sinistral lineation rotated 180° around an axis dipping 60/330.

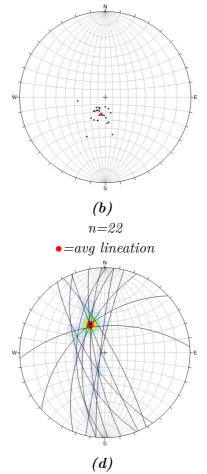




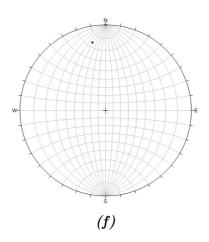








n=13





(a) Sinistral fold deforming the VSZ mylonitic foliation, cut by later brittle fault.



(c) Sinistral fold of a strongly mylonitic felsic layer.



(e) External foliation cut by sheared foliation (red) with sinistral kinematics.



(b) Sinistral σ -clast hosted in a mylonitic band.



(d) Leptitic gneiss affected by the VSZ sheared foliation wrapping around mafic clasts.



(f) External foliation cut by sheared foliation (red) with dextral kinematics.

Figure 4.10 – Kinematic indicators from Væleren Shear Zone. Photo (a) and (b) from (UTM32N 558029 - 6663062, (c) from (UTM32N 558036 - 6663108), (d) from (UTM32N 557998 - 6663546), (e) from (UTM32N 558067 - 6663939) <u>68</u>d (f) from (UTM32N 557823 - 6661147)

Effects of folding of the stretching lineation

Folding of an existing shear zone can cause an inversion of the sense of shear. As described by Goscombe and Trouw (1999), this is a function of the relationship between the fold axis and the pre-existing stretching lineation. If the angle between the two ϕ is between 0° and 45°, then there is an inversion in sense of shear in overturned flanks due to folding. And for ϕ between 45° and 90°, the sense of shear is the same on alternate limbs. In the case of the folded shear plane of the VSZ ϕ has a value of 36° to 77° with an average of 50° . The relative big scatter in lineation measurements is, as described previously, due to the heterogeneous lithological composition of the sheared rock package. This spread is distributed in such a way that some lineations will have an angle $\phi < 45^{\circ}$ while some $\phi > 45^{\circ}$, there should thus be evidence of both senses of shear in the overturned flank. This is the only effective way to determine which of the flanks displays the original tectonic transport sense if the study is done in a limited area (as it is the case). It is therefore difficult to conclude if the original (pre folding) sense of shear is dextral strike-slip on a vertical shear plane or a reverse dip-slip (Figure 4.11).

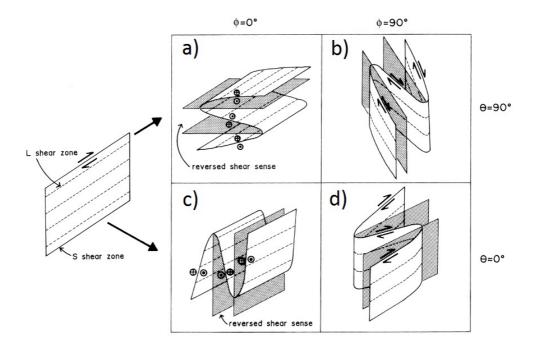


Figure 4.11 – The figure show an illustration of the two endmembers found in VZS. The folding can be classified to a state somewhere between (c) and (d) (keep in mind the figures should be rotated 90° in order for lineations to be vertical) where $\phi < 45^{\circ}$. Figure from Goscombe and Trouw (1999).

Dikes of Væleren Shear Zone

There are three generations of intrusives within the VZS, labelled Generation 1 through 3, with Generation 1 being the oldest (Figure 4.12). They are separated by both visual appearance, mineralogy and level of deformation. The 1st generation contains the most deformed dikes. Generation 1 dykes are extremely transposed along the mylonitic foliation. They vary in thickness between ca. 5 and ca. 15 cm. They appear as highly disrupted trains of clasts of mafic material embedded in a finer felsic groundmass, itself strongly sheared within the VSZ. The clasts are aligned parallel to the mylonitic foliation trend and their spatial arrangement defines the shape of the dykes (Figure 4.12e). The mafic clasts consist of amphibibole, pyroxenes and plagioclase. There are some larger grains of clinopyroxene that are interpreted to be igneous phases that are partly altered to amphibole. High strain samples contain more orthopyroxene whereas lower strain samples show almost no pyroxene and mainly amphibole and plagioclase. There is a strong foliation visible in thin section, but only samples that show high strain display a visible foliation in hand specimen. In most outcrops, generation 1 dykes are affected by isoclinal folds with steep axes oriented on average 76° toward 180° . The folds display very long, highly stretched limbs ca. 5 cm thick and thickened fold hinges. But, as seen in Figure 4.12e and 4.12f, transposition is such that limbs are not necessarily always connected, with rootless folds being thus common.

Generation 2 dykes are very fine grained. They are dark in color and contain abundant and distinctive garnets. These reddish garnet aggregates (Figure 4.12c and 4.12d) appear to be also strung out parallel to the stretching lineation. The composition of the dikes is given by amphibole and plagioclase, but also some coarser igneous clinopyroxene partly altered to amphibole. The width of the second generation dikes is different from the first. It can range from cm-scale up to 5 dm. Generation 2 dykes are locally observed to cut through discordantly the hinges of the isoclinal folds affecting generation 1 dykes (Figure 4.12e). However, they are themselves isoclinally folded. Generation 2 dykes are not nearly as transposed as those of generation 1. Dikes of both generations have the same folding geometry and style, with isoclinal folds with steep to subvertical fold axis. All this suggests that first generation dikes intruded, were heavily transposed and folded isoclinally before generation 2 dikes intruded. A second and almost coaxial isoclinal folding event then occured. The regional shear foliation with lineations is present in the first generation dike but has not been observed in the second. This could indicate that mylonitic fabric of the host rock formed between the two intrusive events. Both generations have a strike that is more or less parallel with the VSZ shear foliation but the second generation seems to cut the foliation more than being a part of it (Figure 4.12c and 4.12d), as is the case for the first generation.

One single, highly discordant dyke does not show the same orientation as the first or second generation. It is an EW-striking potassium rich lamprophyre dike and it cuts almost perpendicularly the VSZ mylonitic fabric. It is not folded and does not show any pervasive sign of ductile deformation. It is however offset by a N-S striking brittle fault that is reactivated along the sheared foliation. Sample BBI138 from the dyke was dated (see U-Pb geochronology section).



(a) Isoclinally folded 2^{st} generation dike.



(c) 2^{nd} generation dike rich in garnets



(e) 1^{st} and 2^{nd} generation dike. Notice 2^{nd} generation cutting heavily transposed 1^{st} generation.



(b) Isoclinally folded 2st generation dike.



(d) 3 dm wide2nd generation dike cutting heavily sheared hostrock.



(f) 1^{st} and 2^{nd} generation dike. Notice 2^{nd} generation cutting heavily transposed 1^{st} generation.

Figure 4.12 – Photos of 1st and 2nd generation dikes. Photo (a) and (b) from (UTM32N 558060 - 6663212), (c) from (UTM32N 557804 - 6661743), (d) from (UTM32N 558032 - 6663056), (e) and (f) from (UTM32N 557994 - 6663247).

The brittle structures found in investigated area

The brittle history obviously postdates all ductile deformation of proterozoic age. Some of the sheared N-S foliation surfaces show evidence of brittle extensional reactivation with E-W extension (Figure 4.13). There are also a set of E-W fault planes suggesting a separate N-S extension phase. All fracture planes are recognized in the topography. Figure 4.13 shows the produced lithological map on top of a DTM (digital terrain model) derived from a digital elevation model. The dominating directions of the lineaments coincides with measurements of brittle features i.e. E-W and N-S striking faults.

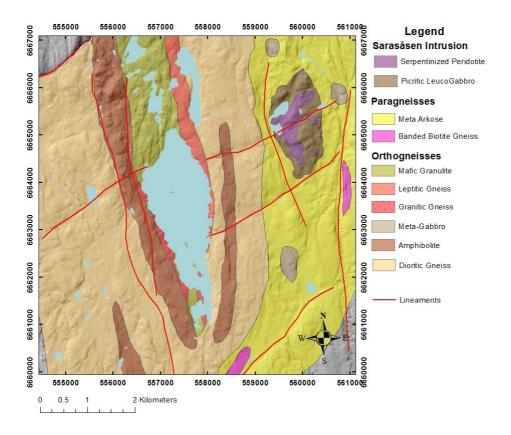


Figure 4.13 – Lineaments drawn from remote sensing.

4.5 Geophysical investigation

4.5.1 Filtering and data enhancement

In order to enhance the signal sources of the anomaly grids a range of high-pass and low-pass filters were applied. The filters applied to the magnetic grid are low-pass filter with 5000 m cut-off wavelength, total horizontal gradient (THDR), first vertical gradient (1VD), analytic signal (AnSig) and tilt derivative (TDR). The gravity grid was enhanced by only applying high- and low-pass wavelength filtering. All magnetic grids are shaded with light inclination of 45 degrees from the NE.

Wavelength filtering

The used magnetic grid contains mainly low wavelength signals so highpass filtering did not reveal anything new. However a low-pass filtering with cut-off wavelength of 5000 m (Figure 4.14) revealed signals from sources with a depth of 1500 m or more. Due to the ambiguity of wavelength distribution and signal source shape, this is not necessary the case since shallow large sources also can produce large wavelengths. But it is a good estimate. After removing the shallow, short wavelength surface signals, four major highs are revealed. When comparing to geological maps the NW and SE highs match known outcropping gabbroic intrusions. The other two could relate to subsurface intrusions of the same nature.

The gravity signal behaves differently. The type of gravity survey used in this study produces data dominated by long wavelength. This is because the detail level of the survey does not allow detection of short wavelengths due to low sampling frequency. But an investigation of deep seated crustal sources and crustal thickness can be done. In order to enhance the deeper sources a cut-off wavelength of 60 km was chosen for both high- and low-pass filters (Figure 4.16 and 4.15). The high-pass grid produced displays wavelengths of 60 km and less, which translates into a depth including all signals down to 20 km. These numbers are only an estimate based on the relation between signal wavelength and source depth. Before interpreting the gravity grid, the distance between the measurements must be considered. There are places with a very low density of measurements which could affect the quality of the gridding. As an example, in the NW there is a gravity high in an area with almost no measurements (Figure 3.2), which is probably only an interpolation artefact. This area also displays a high in the high-pass grid, also an artefact (Figure 4.16).

Analysis of the high-pass grid reveals two highs in the centre and SW. They can both be related to outcropping gabbros just outside the Oslograben in the proterozoic gneisses. West of the highs is a low trending N-S that can be related to the major shear zone separating the Kongsberg terrane from Telemarkia. The northern high is situated on sedimentary rocks and the eastern N-S trending low on felsic intrusions, both in the Oslo-graben. There are also two circular lows in the southern part, these are also associated with a felsic intrusion in the Oslo-graben. Petrophysical investigations of the area also confirms this density contrast, with the felsic intrusions having a density of less than 2600 kg/m^3 and the sedimentary rock being more dense with values ranging above 2700 kg/m^3 .

The low-pass grid reveals anomalies from deeper parts of the crust. It reveals one single large high. It could be a deep situated pluton in the oslo-graben or even an up-welling of the mantle.

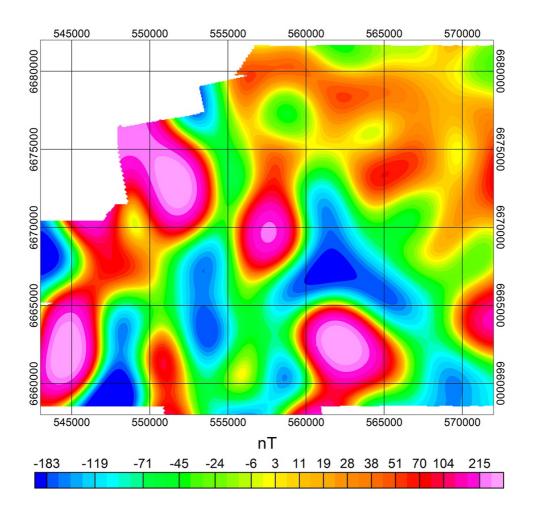


Figure 4.14 – Low-pass filtered magnetic grid with cut-off wavelength of 5000 m.

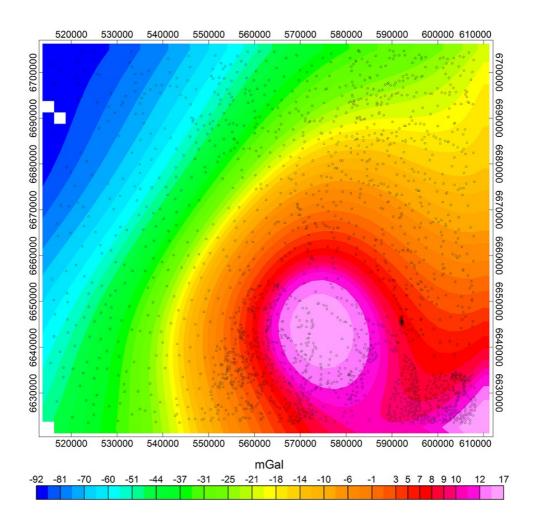


Figure 4.15 – Low-pass filtered gravity grid with cut-off wavelength of 60 km.

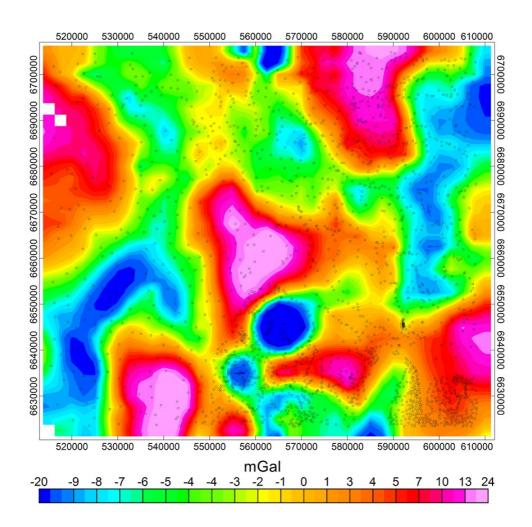


Figure 4.16 – High-pass filtered gravity grid with cut-off wavelength of 60 km.

Horizontal Derivatives

The total horizontal derivative grid is a visualization of where the horizontal gradient is highest. For an anomaly source with vertical edges the gradient will be highest at the edge, which in turn makes the THDR an edge-enhancing filter.

The magnetic THDR (Figure 4.17) is considerably noisier than the anomaly grid, and the other enhancements. All wavelengths lower than 100 m can be neglected due to them being below the Nyquist wavelength. Even longer wavelengths can be neglected in the Y direction due to the undersampling caused by the flight-line spacing. This undersampling is visible in the eastern parts of the grid with artefacts across flightlines dominating the grid.

The SW is dominated by N-S trending anomalies. This is also reflected in the geology with N-S striking features reflecting the locally strong compositional banding. The central high visible on the low-pass image shows some irregular edges which does not necessary correlate with the geometry of an intrusion.

Since the grid consists of several closely spaced narrow bodies, the gridding process becomes extremely ambiguous. The vertical derivatives which peaks over the tops of the sources will be more suited in such areas when interpreting the lateral extent of the anomaly source.

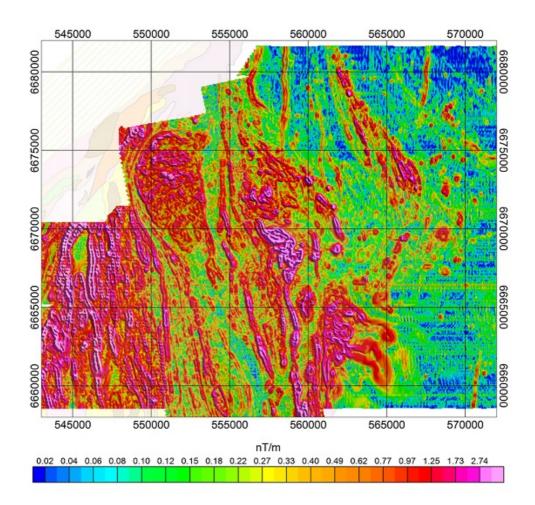


Figure 4.17 – THDR of the magnetic grid.

First Vertical Derivative

The 1VD (Figure 4.18) is a visualization of the vertical change in the magnetic field. This causes it to return maximum values on top of the anomaly, passes through zero on the edges, and is negative outside (Figure 3.7. These properties makes the 1VD a powerful tool for displaying efficiently the lateral extent of a source.

The eastern side of the grid is dominated by across flightlines artefacts, probably due to undersampling. But also along flightline artefacts are present in central and western parts. This is probably due to poor levelling of flightlines.

The NW gabbro is also visible. However there are now some parallel "valleys" trending NE-SW. These valleys matches perfectly with topographic valleys. The topographic difference is 20-60 m, but since the survey is flown with helicopter there is no reason to believe that the low is due to different ground clearance. More likely is lithological differences that causes both magnetic lows and erosion due to lithologic weakness. The SW area reveals several N-S trending, narrow anomalies. There seems to be an repetition in anomalies around possible antiform isoclinal folding. The anomalies also seems to bend around the large NW gabbro, indication possible shearing with the gabbro being a large scale porphyroclast. The shape of the central high from the low-pass grid does not have a typical intrusion body signature. It could be complex folding of the N-S trending high that merges with the complex area. The central area is dominated with irregular shape anomalies compared to the western area.

The N-S trending anomalies are barely represented in published geological maps.

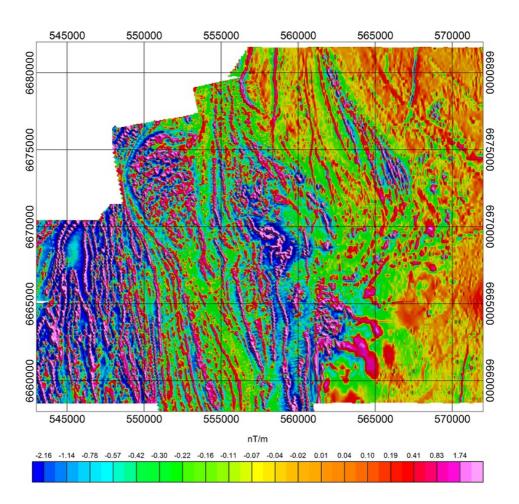


Figure 4.18 – 1VD of magnetic grid.

Analytic Signal

AnSig (Figure 4.19) is the vector sum of the three directional derivatives. The signal is ideally symmetrical with peaks over the edges of wide bodies and over the center of narrow bodies (Milligan and Gunn, 1997). It has more useful purpose in areas with low field inclination as it effectively maps edges of the magnetic body irrespective the presence of non-induced magnetism (Isles and Rankin, 2013). This is not an issue since the investigated area is situated in an area of almost vertical inclination.

The western area that showed closely spaced N-S trending anoma-

lies in 1VD now show indistinguishable highs. The area is also riddled with along flight-line artefacts. Both gabbros previously described are also clearly visible but in this case the AnSig filter does not contribute anything that the previously filters does not cover.

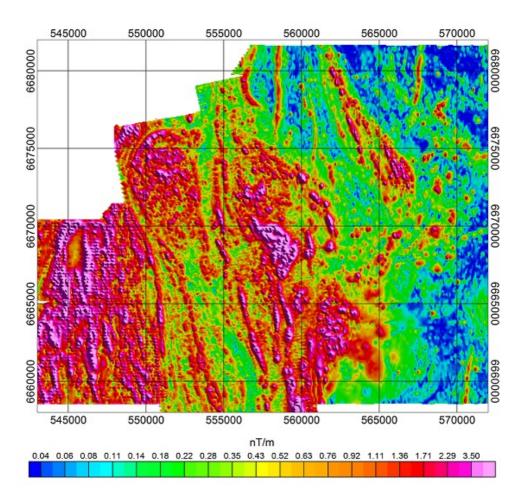


Figure 4.19 – Analytic signal of magnetic grid.

Tilt Derivative

TDR (Figure 4.20) is the arctan of the ratio of 1VD and THDR, it was first described by Miller and Singh (1994). It produces a similar image to 1VD, however it normalizes depth of anomalies so both shallow and deeper anomalies are displayed similarly. It also has the advantage of being negative outside the anomaly, thus making it easy to display only positive returns. This produces a cleaner image of lateral dimensions of the sources.

In the case of this investigation the TDR does not give any clear advantages over 1VD. Maybe the N-S trending anomalies are more prominent and easier to track. It is also clean of along flightline noise in the central section. However, since the negative returns are removed, more "open space" is left in the image. This makes it possible to use a geological map as background

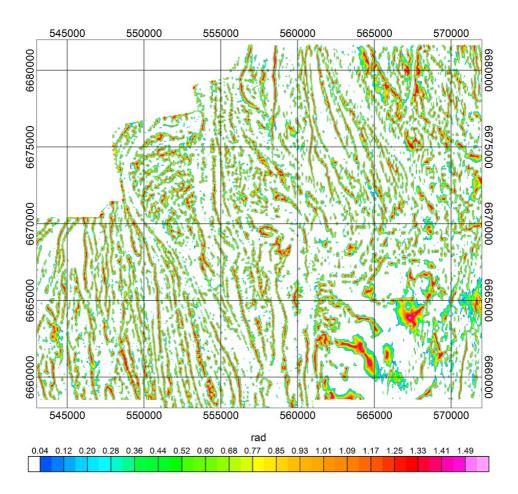


Figure 4.20 – Positive returns of TDR of magnetic grid.

4.5.2 Petrophysics

Table 4.3 – Selection of rocks from investigated area, presented with density, susceptibility, induced magnetism (J_i) remanence (J_r) and Q-value (J_r/J_i) .

Layer	Density	Susc SI	J_i [nT]	$J_r [nT]$	Q-value
	$[kg/m^3]$				
Oslo-Graben Intrusives:					
Granite	2585	0.009795	499.5	207.9	0.41
Granite	2578	0.017776	906.6	215.6	0.24
Granite	2578	0.008300	423,3	11.8	0,03
Monzonite	2715	0.009346	476.6	76.3	0.16
Syenite	2599	0.027241	1389.3	466.7	0.34
Syenite	2627	0.017604	897.8	85.4	$0,\!10$
Syenite	2611	0.030164	1538,4	382.6	0.25
Oslo-Graben Sedimentary:					
Limestone	2693	0.000151	7.7	13.5	1.8
Limestone	2715	0.000138	7	10.7	1.5
Limestone	2702	0.000082	4.2	12.2	2.9
Pelite	2744	0.000282	14.4	35	2.4
Pelite	2765	0.000605	30.9	12.1	0.39
Sandstone	2643	0.000035	1.8	0	0
Mica Schist	2984	0.001222	62.3	0	0
Proterozoic Rocks:					
Dioritic Gneiss	2811	0.000303	15.5	16.9	1.1
Horneblende-Gneiss	2816	0.000343	17.5	0	0
Horneblende-Gneiss	2837	0.000443	22.6	10.7	0.47
Mica Gneiss	2779	0.000217	11.1	13.7	1.23
Mica Gneiss	2712	0.000124	6.3	13.9	2.2
Amphibolite	3009	0.000838	42.7	4.9	0.11
Granodioritic Gneiss	2765	0.000227	11.6	11.9	1.03
Granodioritic Gneiss	2750	0.000229	11.7	4.3	0.37
Granodioritic Gneiss	2749	0.000188	9.6	0	0
Granodioritic Gneiss	2748	0.000157	8	0	0
Mica Schist	2861	0.046115	2351.9	0	0
Granitic Gneiss	2682	0.000272	13.9	0	0
Gabbro	2945	0.000555	28.3	12.6	0.44
Quartzite	2646	0.000083	4.2	0	0
Amphibolite	3067	0.000716	36.5	5.1	0.14
Gabbro	3083	0.015243	777.4	2812.8	3.62
Gabbro	2939	0.042617	2173.5	443.7	0.20
Granitic Gneiss	2696	0.023560	1201.6	0	0

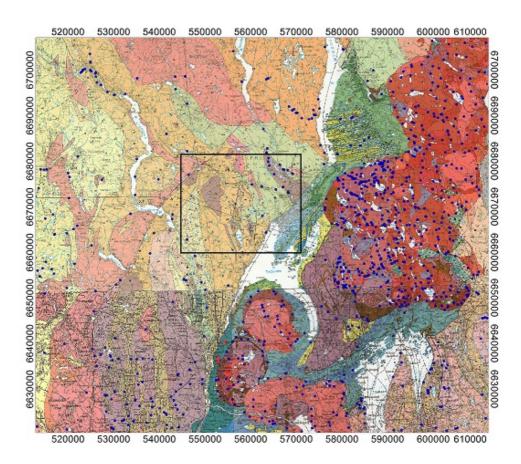


Figure 4.21 – Samples from investigated area from NGU's petrophysical database. Highlighted area covers magnetic surveys.

Oslo-Graben

Table 4.3 is divided in three areas; Oslo-graben intrusives, Oslo-graben sedimentary rocks and proterozoic rocks. The first two areas are only covered by the gravimetric survey.

As seen on the gravimetric grids, there are some large gravity lows associated with intrusive rock and highs with sedimentary rocks. This is confirmed by the density of the rocks in question. The lowest anomaly in Figure 13, circular shaped in the center, corresponds to a granitic intrusion. This is also reflected in the density of the granite samples. The central low in Figure 4.16 is associated with syenitic intrusions, also reflected by the density readings. The northern gravity high corresponds with sedimentary rocks. Looking at Table 4.3 their density is indeed higher than the intrusives, causing a gravity high.

Proterozoic rocks

The central gravity high associated to outcropping gabbroic intrusions cannot be compared to the petrophysic table due to lacking data. There are only two samples from this area, a mica schist from the lakeshore and a gabbro north of the schist (Figure 4.21), both with higher densities than surrounding gneisses. The southwestern high is also associated with outcropping gabbroic intrusions. This is confirmed by samples from the area. The bottom three samples in Table 4.3 are all from this area.

The lack of samples in the magnetic area prevents good statistic on susceptibility, remanence and density. Only the north-eastern area is well covered. This means that no reasonable overview of induced and remanent magnetism can be presented.

Chapter 5

Discussion

The leucogabbro and peridotite of the Sarasåsen intrusion show a very homogeneous olivine and pyroxene composition (Figure 4.7). This suggests that the Sarasåsen intrusion was crystallized from one batch of magma and the ultramafic portion of it represents a cumulus at the bottom of the magma chamber. Aeromagnetic investigations revealed a shallow root of the intrusion based on the short wavelength of its anomaly signature. This indicates that the outcropping intrusion is the lower remains of a larger magma chamber whose top is now eroded. Feeder dikes are likely to extend to great depth below the present erosional level. The fact that foliated xenoliths of the host rock types are found within the intrusion suggests the Sarasåsen intrusion to have been emplaced after the main regional fabric-forming event in the area. This conclusion is further supported by the generally undeformed nature of the intrusion compared to, for example, the well foliated 1224 ± 15 Ma (Munz and Morvik, 1991) meta-gabbros present within the Kongsberg terrane (Munz and Morvik, 1991; Starmer, 1985). Since no direct geochronology constraints on the Sarasåsen intrusion are available as yet, only indirect relationships can be established.

The serpentinized fractures within the Sarasåsen peridotites are not randomly oriented, but, since no systematic collection of oriented samples from the intrusion was done, no structural implications can be elaborated. The volume expanding nature of serpentinization has caused the plagioclase surrounding olivine to fracture radially from olivine grains. The pressure exerted by the growing serpentine mineral can be as high as 100 MPa (Steiger, 2005). Stable conditions for lizardite crystallization are between 200 and 300°C and 70 MPa (Grauby et al., 1998). This indicates zeolite facies conditions. However there are prehnite and pumpellyite along fractures in plagioclase. The alteration from plagioclase to this mineral assemblage requires higher pressure conditions than zeolite facies,(Figure 5.1). This suggests in turn that the Sarasåsen intrusion also experienced a period of zeolite facies metamorphism during which fracturing and serpentinization occurred. Moreover, the presence of prehnite and pumpellyite suggests higher PT conditions, indicative of a distinct metamorphic event after serpentinization started.

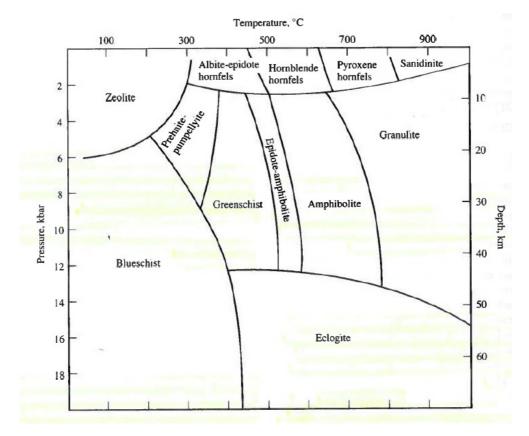


Figure 5.1 – Metamorphic facies in PT diagram. From Blatt et al. (2006), page 344.

Any model of the evolution of the area of interest has to necessarily

take account of the existence of the hitherto unknown Væleren Shear Zone (VSZ) and the role it may have played in juxtaposing the mapped lithologies. On the eastern side of Lake Væleren, the VSZ bears steeply S-plunging stretching lineations on subvertical foliation surfaces that dip predominantly west (albeit some significant scatter). Associated kinematic indicators constrain a component of sinistral shear on map view. Along the western coast line of the lake, however, the VSZ is characterised by subhorizontal N-plunging lineations on subvertical foliation surfaces and a component of dextral shear. This difference can be explained by either multiple reactivation of the shear fabric (wherein part of the mylonite zone was reactivated under different kinematic conditions) or by tight- to isoclinal folding of the VSZ foliation around a steeply NWplunging fold axis. Structural mapping does indeed reveal the presence of folds that can account for the folding of the shear fabric. If the subvertical lineation on the eastern side of Lake Væleren represents the original stretching direction of the VSZ and one works with the present-day attitude of the foliation, the eastern block would then represent the footwall and the western block the hanging wall to a oblique sinistral transtensional shear zone. This would imply exhumation of the eastern block relative to the western. Shearing would be also pre-folding. Caution is, needed, however because of the very steep attitude of the mylonitic foliation planes. An average dip to the east, for example, would result in significantly different kinematics.

An alternative is that it is the western flank that represents the original pre-folding kinematics and shear zone orientation, in which case the VSZ would be a steep dextral strike-slip shear-zone.

Finally, one also has to consider the possibility that neither scenarios are representative and geologically meaningful in that shearing took place along a completely differently oriented mylonitic fabric. The present orientation and the VSZ "apparent" kinematic framework would thus result from shortening and transposition postdating the main VSZ shearing episode, such that any conclusion as to the original tectonic significance of the VSZ is precluded. It can be mentioned, however, that comparison of my results with the results of a large study of the Kongsberg and Modum terranes run by the NGU (KONGMO project, Viola et al.) supports the possible interpretation of the VSZ as a sinistral shear zone. In fact, the KONGMO project has documented numerous examples of steep shear zones characterised by overall sinistral kinematics, whereas dextral sense of shear is less common. These remain only speculations and more detailed studies and generation of tighter geochronological constraints are necessary to generate a more robust conceptual scheme.

The geochronological work by Dr. Bernard Bingen on samples from the mapped area within the framework of the NGU KONGMO project helps nonetheless to add robust time constraints to at least part of the geological evolution of the investigated region. In detail, the 1036 Ma U-Pb zircon age of the EW striking lamprophyre dyke cutting the VSZ constrains the entire ductile deformation to pre 1036 ± 9 Ma (Figure 4.8b). According to the model proposed by Bingen et al. (2008b) Telemarkia in the west was experiencing a period of crustal thickening from 1035 to 980 Ma, called the Agder phase. However in the east the Idefjorden terrane was experiencing unroofing and possible exhumation. This would be consistent with the exhumation of the eastern block during the VSZ event. This exhumation must have ceased before the 1036 intrusive event. It is uncertain whether the Sarasåsen intrusion was emplaced before the VSZ event. It is clear that the block hosting the intrusion must have undergone exhumation in order to expose the lower remains of the magma chamber.

Chapter 6 Conclusions

The study of the Væleren - Sarasåsen area has now put some constraints in terms of geochronology. Origin of the ultramafic Sarasåsen intrusion has also been established. A geological evolution based on earlier models and my own research has now been established.

- The oldest rocks in the area are the orthogneisses. U-Pb geochronology data has revealed zircon ages of ca. 1720, 1650 and 1578 Ma, meaning sedimentation post 1578 Ma.
- U-Pb data from the leptitic gneisses reveal an igneous age of 1538 Ma. The leptitic gneiss is interpreted to be the high strain result with the granitic gneiss as protolith. The emplacement of the granitic body found on the eastern shore of Lake Væleren intruded into the sedimentary unit.
- The voluminous dioritic intrusion is intruded after the granitic magmatism. It has no U-Pb geochronology so no direct age is established. It contains layers of amphibolites which are concluded to be mafic horizons within the magmachamber.
- A period of hiatus has then followed, ending in eruptive event when basaltic lava erupted and deposited on top of dioritic intrusion. Gabbroic intrusions hosted in the meta-sediments are believed to be simultaneous as the mafic eruptives. First generation dikes of VSZ are also associated with this intrusive event.

- During the Sveconorwegian orogeny all rocks are metamorphosed. The regional foliation of the rocks is formed. Metamorphism peaked in granulite facies with the basalt metamorphosed to a mafic granulite. The VSZ is also active during an exhuming event during the Agder phase (Bingen et al., 2008b). After exhuming the area again undergoes E-W compression and the large-scale isoclinal folding of VSZ occurs.
- The E-W striking lamprophyre dike cuts the VSZ fabric at ca 1032 Ma, sealing all deformation in VSZ to pre intrusive.
- The Sarasåsen intrusion is intruded in association with the lamprophyre dyke or in a separate younger igneous event. This intrusive event is not associated with an ophiolite complex, but is the result of a basaltic intrusion. Based on alteration processes recorded in Sarasåsen intrusion, one episode of zeolite facies alteration (serpentinization) and one subsequential prehnite-pumpellyite facies metamorphism event occurred.

Chapter 7 Perspectives and future work

This thesis investigates the Væleren - Sarasåsen area by using geophysical, petrological, geochemistral and structural methods. These methods in themselves are so complex that one could write a thesis on each subject. Therefore a more detailed study of each field would have been optimal.

- The geophysical investigation is limited to 2D-filtering of gravity and aeromagnetic data. In this regard I would suggest further reduction of magnetic data in the area in question. By doing petrophysical analyses of samples taken from the area, remanent magnetization could be mapped. Doing this would strengthen any geophysical modelling since unaccounted remanent magnetization causes difficulties during 3D modelling.
- Further mapping of the VSZ is required to understand its relationship with the regional structures. No analyses of micro-structures was done in this thesis, something that would enhance the understanding of the mechanics in process during high strain events.

References

- Andersen, T., Andresen, A., and Sylvester, A. G. (2001). Nature and distribution of deep crustal reservoirs in the southwestern part of the Baltic shield: evidence from Nd, Sr and Pb isotope data on late Sveconorwegian granites. *Journal of the Geological Society, London*, 158:253–267.
- Andersson, U. B., Neymark, L. A., and Billström, K. (2002). Petrogenesis of Mesoproterozoic (Subjotnian) rapakivi complexes of central Sweden: implications for U-Pb zircon ages, Nd, Sr and Pb isotopes. *Transactions of the Royal Society of Edinburgh: Earth Sciences*, 92:201–228.
- Austin Hegardt, E., Cornell, D. H., Hellström, F. A., and Lundquist, I. (2007). Emplacement age of the mid-proterozoic kungsbacka bimodal suite, sw sweden. *GFF*, 129:227–234.
- Auwera, J. V., Bogaerts, M., Liégeois, J. P., Demaiffe, D., Wilmart, E., Bolle, O., and Duchesne, J. C. (2003). Derivation of the 1.0–0.9 Ga ferro-potassic A-type granitoids of southern Norway by extreme differentiation from basic magmas. *Precambrian Research*, 124:107– 148.
- Berglund, J., Larson, S. A., and Vinnefors, A. (1997). Sveconorwegian extension-parallel deformation structures; an example from the Hammarö Shear Zone, SW Sweden. *GFF*, 119:169–180.
- Bingen, B., Birkeland, A., Nordgulen, O., and Sigmond, E. M. O. (2001). Correlation of supracrustal sequences and origin of terranes in the Sveconorwegian orogen of SW Scandinavia: SIMS data on zircon in clastic metasediments. *Precambrian Research*, 108:293–318.

- Bingen, B., Boven, A., Punzalan, L., Wijbrans, J., and Demaiffe, D. (1998). Hornblende 40Ar/39Ar geochronology across terrane boundaries in the Sveconorwegian province of S Norway. *Precambrian Re*search, 90:159–185.
- Bingen, B., Davis, W. J., Hamilton, M. A., Engvik, A., Stein, H. J., Skår, O., and Nordgulen, O. (2008a). Geochronology of high-grade metamorphism in the Sveconorwegian belt, S Norway: U-Pb, Th-Pb and Re- Os data. *Norwegian Journal of Geology*, 88:13–42.
- Bingen, B., Mansfeld, J., Sigmond, E. M. O., and Stein, H. J. (2002). Baltica–Laurentia link during the Mesoproterozoic: 1.27 Ga development of continental basins in the Sveconorwegian Orogen, southern Norway. *Canadian Journal of Earth Sciences*, 39:1425–1440.
- Bingen, B., Nordgulen, O., and Viola, G. (2008b). A four-phase model for the Sveconorwegian orogeny, SW Scandinavia. Norwegian Journal of Geology, 88:43–72.
- Bingen, B., Skår, ., Marker, M., Sigmond, E. M. O., Nordgulen, ., Ragnhildstveit, J., Mansfeld, J., Tucker, R. D., and Liégeois, J. P. (2005). Timing of continental building in the Sveconorwegian orogen, SW Scandinavia. Norwegian Journal of Geology, 85:87–116.
- Bingen, B., Stein, H. J., Bogaerts, M., Bolle, O., and Mansfeld, J. (2006). Molybdenite Re-Os dating constrains gravitational collapse of the Sveconorwegian orogen, SW Scandinavia. *Lithos*, 87:328–346.
- Blatt, H., Tracy, R. J., and Owens, B. E. (2006). *Petrology: Igneous, Sedimentary and Metamorphic.* W. H. Freeman and Company, New York, third edition edition.
- Bogaerts, M., B, S., Liégeois, J. P., and Vander Auwera, J. (2003). Petrology and geochemistry of the Lyngdal granodiorite (Southern Norway) and the role of fractional crystallization in the genesis of Proterozoic ferro-potassic A-type granites. *Precambrian Research*, 124:149–184.
- Bolle, O., Diot, H., and Duchesne, J. C. (2000). Magnetic fabric and deformation in charnockitic igneous rocks of the Bjerkreim-Sokndal

layered intrusion (Rogaland, Southwest Norway). *Journal of Structural Geology*, 22:647–667.

- Bugge, A. (1928). En forkastning i det syd-norske grunnfjell. Norges Geologiske Undersøkelse Bulletin, 130:1–124.
- Cosca, M., Mezger, K., and Essene, E. J. (1998). The Baltica-Laurentia connection: Sveconorwegian (Grenvillian) metamorphism, cooling, and unroofing in the Bamble Sector, Norway. 106:539–552.
- de Haas, G.-J. L. M., Nijland, T. G., Valbracht, P. J., Maijer, C., Verschure, R., and Andersen, T. (2002). Magmatic versus metamorphic origin of olivine-plagioclase coronas. *Contributions to Mineralogy and Petrology*, 143:537–550.
- Deer, W. A., Howie, R. A., and Zussman, J. (1992). An introduction to the Rock-Forming Minerals. Longman Scientific & Technical.
- Demaiffe, D., Weis, D., Michot, J., and Duchesne, J. C. (1986). Isotopic constraints on the genesis of the Rogaland anorthositic suite (SW Norway). *Chemical Geology*, 57:167–179.
- Duchesne, J. C., Maquil, R., and Demaiffe, D. (1985). The Rogaland anorthosites: facts and speculations. In Tobi, A.C. & Touret, J.L.(eds.). The deep Proterozoic crust in the north Atlantic provinces, NATO-ASI C158:449–476.
- Ebbing, J., Afework, Y., Olesen, O., and Nordgulen, O. (2005). Is there evidence for magmatic underplating beneath the Oslo rift? *Terra Nova*, 17:129–134.
- Evans, B. W., Hattori, K., and Baronnet, A. (2013). Serpentinite: What, Why, Where? *Elements*, 9:99–106.
- Goscombe, B. and Trouw, R. (1999). The geometry of folded tectonic shear sense indicators. *Journal of Structural Geology*, 21:123–127.
- Grauby, O., Baronnet, A., Devouard, B., Schoumacker, K., and Demirdijan, I. (1998). The chrysotile-polygonal serpentine suite synthesized

from a $3MgO-2SiO_2$ -excess H_2O gel (abstract). Terra Nova Abstract Supplement, 1:24.

- Hattori, K. H. and Guillot, S. (2007). Geochemical character of serpentinites associated with high- to ultrahigh pressure metamorphic rocks in the Alps, Cuba, and the Himalayas: Recycling of elements in subduction zones. *Geochemistry Geophysics Geosystems*, 8:doi:10.1029/2007GC001594.
- Hellström, F. A., Johansson, A., and Larson, S. A. (2004). Age emplacement of late Sveconorwegian monzogabbroic dykes, SW Sweden. *Precambrian Research*, 128:39–55.
- Isles, D. J. and Rankin, L. R. (2013). Geological Interpretation of Aeromagnetic Data. The Australian Society of Exploration Geophysicists.
- Jacobsen, S. B. and Heier, K. S. (1978). Rb-Sr isotype systematics in the Kongsberg Sector, South Norway. *Lithos*, 11:257–276.
- Jaffrey, A. H., Glendenin, L. E., Bentley, W. C., and Essling, A. M. (1971). Precision measurement of the half-lives and specific activities of U235 and U238. *Physics review*, C4:1889–1907.
- Johannesen, G. A. (1974). Nikkel- og kobberforekomster og bergarter i Tyristrand og Holleia. Master's thesis, Universitetet i Oslo.
- Johansson, L. and Johansson, . (1993). U–pb age of titanite in the Mylonite Zone, southwestern Sweden. Geologiska Föreningens i Stockholm Förhandlingar, 115:1–7.
- Larson, S. ., Cornell, D. H., and Armstrong, R. A. (1999). Emplacement ages and metamorphic overprinting of granitoids in the Sveconorwegian Province in Värmland, Sweden - an ion probe study. *Norsk Geologisk Tidsskrift*, 79:87–96.
- Leake, B. E., Woolley, A. R., Arps, C. E. S., Birch, W. D., Gilbert, M. C., Grice, J. D., Hawthorne, F. C., Kato, A., Kisch, H. J., Krivovivhev, V. G., Linthout, K., Laird, J., Maresch, W. V., Nickel, E. H., Rock, N. M. S., Schumacher, J. C., Stephenson, N. C. N., Whittaker, E. J. W.,

and Youzhi, G. (1997). Nomenclature of amphiboles: report of the subcommittee on amphiboles of the International Mineralogical Association, commision on new minerals and mineral names. *The Canadian Mineralogist*, 35:219–246.

- Ludwig, K. R. (1998). On the treatment of concordant uranium-lead ages. *Geochimica et Cosmochimica Acta*, 62:665–676.
- Ludwig, K. R. (2001). Isoplot/Ex version 2.49, a geochronological toolkit for Microsoft Excel: Berkeley. Berkeley, special publication no. 1a edition.
- Miller, H. G. and Singh, V. (1994). Potential field tilt A new concept for location of potential field sources. *Journal of Applied Geophysics*, 32:213–217.
- Milligan, P. R. and Gunn, P. J. (1997). Enhancement and presentation of airborne geophysical data. AGSO Journal of Australian Geology and Geophysics, 17 issue 2:63–75.
- Möller, C., Andersson, J., Lundqvist, I., and Hellström, F. A. (2007). Linking deformation, migmatite formation and zircon U-Pb geochronology in polymetamorphic gneisses, Sveconorwegian province, Sweden. Journal of Metamorphic Geology, 25:727–750.
- Möller, J. C., Anderson, U. J., Söderlund, U., and Johansson, L. (1997). A Sveconorwegian deformation zone (system?) within the Eastern Segment, Sveconorwegian orogen of SW Sweden — a first report. *GFF*, 119:73–78.
- Mulch, A., Cosca, M. A., Andresen, A., and Fiebig, J. (2005). Time scales of deformation and exhumation in extensional detachment systems determined by high-spatial resolution in situ UV-laser 40Ar/39Ar dating. *Earth and Planetary Science Letters*, 233:375–390.
- Munz, I. A. and Morvik, R. (1991). Metagabbros in the Modum Complex, southern Norway: an important heat source for Sveconorwegian metamorphism. *Precambrian Research*, 52:97–113.

Oftedahl, O. (1980). Geology of norway. Nor Geol. Unders., 356:3-115.

- O'Hanley, D. S. (1996). Serpentinites: Records of Tectonic and Petrologic History. Oxford University Press, Oxford, page 277 pp.
- Olesen, O., Smethurst, M. A., Torsvik, T. H., and Bidstrup, T. (2004). Sveconorwegian igneous complexes beneath the Norwegian-Danish Basin. *Tectonophysics*, 387:105–130.
- Park, R. G., Åhäll, K. I., and Boland, M. P. (1991). The sveconorwegian shearzone network of SW Sweden in relation to mid-Proterozoic plate movements. *Precambrian Research*, 49:245–260.
- Reeves, C. (2005). Aeromagnetic Surveys, Principles, Practice & Interpretation, chapter 4-6. Geosoft.
- Scherstén, A., Larson, S. ., Cornell, D. H., and Stigh, J. (2004). Ion probe dating of a migmatite in sw sweden: the fate of zircon in crustal processes. *Precambrian Research*, 130:251–266.
- Schiellerup, H., Lambert, D. D., Prestvik, T., Robins, B., McBride, J. S., and Larsen, R. B. (2000). Re–os isotopic evidence for a lower crustal origin of massif-type anorthosites. *Nature*, 405:781–784.
- Schärer, U., Wilmart, E., and Duchesne, J. C. (1996). The short duration and anorogenic character of anorthosite magmatism: U-Pb dating of the Rogaland complex, Norway. *Earth and Planetary Science Letters*, 139:335–350.
- Söderlund, U., Jarl, L. G., Persson, P., Stephens, M. B., and Wahlgren, C. H. (1999). Protolith ages and timing of deformation in the eastern, marginal part of the Sveconorwegian orogen, southwestern Sweden. *Precambrian Research*, 94:29–48.
- Söderlund, U., Möller, C., Andersson, J., Johansson, L., and Whitehouse, M. J. (2002). Zircon geochronology in polymetamorphic gneisses in the Sveconorwgian orogen, SW Sweden: ion microprobe evidence for 1.46-1.42 Ga and 0.98-0.96 Ga reworking. *Precambrian Research*, 113:193– 225.

- Sigmond, E. M. O. (2003). Geologisk kart over Norge, berggrunnskart Odda, 1:250000. Norges geologiske undersøkelse, Trondheim. Skår, Ø. & Pedersen, R.B. 2003: Relations between granitoid magmatism and migmatization: U-Pb geochronological evidence from the Western Gneiss Complex, Norway. Journal of the Geological Society, London, 160:935–946.
- Starmer, I. C. (1977). The geology and evolution of the southwestern part of the Kongsberg Series. *Norsk geologisk Tidsskrift*, 57:1–22.
- Starmer, I. C. (1985). The evolution of the South Norwegian Proterozoic as revealed by the Major and Mega-Tectonics of the Kongsberg and Bamble Sectors. *The Deep Proterozoic Crust in the North Atlantic Provinces*, pages 259–290.
- Steiger, M. (2005). Crystal growth in porous materials—I: The crystallization pressure of large crystals. *Journal of Crystal Growth*, 282:455– 469.
- Stephens, M. B., Wahlgren, C. H., Weijermars, R., and Cruden, A. R. (1996). Left lateral transpressive deformation and its tectonic implications, Sveconorwegian Orogen, Baltic Shield, Southwestern Sweden. *Precambrian Research*, 79:261–279.
- Vander Auwara, J., Bogaerts, M., Liégeois, J. P., Demaiffe, D., Wilmart, E., Bolle, O., and Duchesne, J. C. (2003). Derivation of the 1.0–0.9 Ga ferro-potassic A-type granitoids of southern Norway by extreme differentiation from basic magmas. *Precambrian Research*, 124:107– 148.
- Viola, G., Henderson, I. H. C., Bingen, B., and Hendriks, B. W. H. (2011). The Grenvillian-Sveconorwegian orogeny in Fennoscandia: Backthrusting and extensional shearing along the "Mylonite Zone". *Precambrian Research*, Vol 189:368–388.
- Whitehouse, M. J. and Kamber, B. S. (2005). Assigning dates to thin gneissic veins in high-grade metamorphic terranes: a cautionary tale from Akilia, Southwest Greenland. *Journal of Petrology*, 46:291–318.

- Whitehouse, M. J., Kamber, B. S., and Moorbath, S. (1999). Age significance of U-Th-Pb zircon data from early Archaean rocks of west Greenland – a reassessment based on combined ion-microprobe and imaging studies. *Chemical Geology*, 160:201–224.
- Wiedenbeck, M., Allé, P., Corfu, F., Griffin, W. L., Meier, M., Oberli, F., Von Quadt, A., Roddick, J. C., and Spiegel, W. (1995). Three natural zircon standards for U-Th-Pb, Lu-Hf, trace element and REE analyses. *Geostandards Newsletter*, 19:1–23.
- Zwaan, K. B. and Larsen, B. T. (2003). Berggrunnskart Hønefoss1815 III, M 1:50.000. Norges Geologiske Undersøkelse.

Appendices

Appendix A

Samples

Table A.1 – Overview of all samples taken and their coordinates in UTM32N.

Sample	Easting	Northing	Sample	Easting	Northing
BLA-1	558650	6665412	BLA-100	558769.3	6660228
BLA-2	560311.7	6664991	BLA-101	558802.6	6663972
BLA-3	560094.7	6665340	BLA-102	558540.1	6664007
BLA-4	560154.4	6665351	BLA-103	558342.4	6663937
BLA-5	560161.6	6665538	BLA-104	558112	6664049
BLA-6	559722.4	6665876	BLA-105	555819.5	6664905
BLA-7	559999.9	6665665	BLA-106	556388.7	6665816
BLA-8	560034.1	6665618	BLA-107	557625.6	6665235
BLA-9	558230.8	6659705	BLA-108	557218.5	6665891
BLA-10	557993.8	6663247	BLA-109	557228.9	6665879
BLA-11	557993.8	6663247	BLA-110	557513.2	6665520
BLA-12	557993.8	6663247	BLA-111	559402.8	6662217
BLA-13	560103.4	6665392	BLA-112	559243.6	6662528
BLA-14	560110.9	6665387	BLA-113	556704	6662409
BLA-15	560093.3	6665410	BLA-114	558076.7	6662753
BLA-17	560093.3	6665410	BLA-115	557951.3	6662423
BLA-16	560093.3	6665410	BLA-116	558059.1	6663025
BLA-18	560090.1	6665416	BLA-117	558034	6663059
BLA-19	560082.1	6665434	BLA-118	556590.7	6664140
BLA-20	560073.4	6665438	BLA-119	559128.6	6666138
BLA-21	560069.9	6665452	BLA-120	558948.1	6666499
BLA-22	560061.9	6665463	BLA-121	559252.7	6666811
BLA-23	560931.2	6664938	BLA-122	559437.4	6666996
BLA-24	557477.7	6661825	BLA-123	559152.6	6665220
			BLA-124	559741.1	6666707
			BLA-125	560303.1	6664578

Appendix B Sarasåsen intrusion

B.1 Anhydrous Minerals

m sample BLA-13. Oxides are in $wt\%$ and m

Ola	Ola	Ola	Ola	Pl^{a}	Pl^{a}	Pl^a	Opx ^c	Opx ^c	Am
					1	•	-	-	
55/1	57/1	68/1	69/1	60/1	61/1	75/1	58/1	72/1	50/1
9.21	39.25	39.96	39.87	47.28	46.99	47.13	55.05	56.53	57.40
0.02	0.00	0.06	0.05	32.97	32.77	33.99	1.74	1.17	1.68
0.00	0.00	0.03	0.00	16.67	16.94	17.55	1.02	0.23	13.19
6.18	15.84	15.80	14.99	0.06	0.07	0.08			
0.20	0.19	0.20	0.13	0.00	0.00	0.02	0.25	0.21	0.18
0.00	0.00	0.02	0.02	0.01	0.01	0.03	0.30	0.07	0.02
4.48	44.66	44.33	44.46	0.00	0.00	0.01	31.12	31.67	23.30
0.00	0.00	0.00	0.00	2.34	2.07	1.76	0.02	0.00	0.18
0.01	0.00	0.00	0.00	0.02	0.01	0.01	0.00	0.00	0.01
0.02	0.00	0.07	0.01	0.06	0.02	0.00	0.68	0.04	0.02
0.20	0.27	0.23	0.26	0.02	0.00	0.02	0.01	0.05	0.02
							9.27	10.17	0.00
							1.37	0.00	2.60
	100.19	100.68	99.79	99.43	98.88	100.61	100.72	100.14	98.61
0.98	0.98	0.99	1.00	2.17	2.17	2.14	1.93	1.98	7.767
0.00	0.00	0.00	0.00	1.81	1.81	1.84	0.07	0.05	0.268
				0.83	0.85	0.87	0.04	0.01	1.912
0.34	0.34	0.33	0.32	0.00	0.00	0.00			
0.00	0.00	0.00	0.00	0.00	0.00	0.00	0.01	0.01	0.021
				0.00	0.00	0.00	0.01	0.00	0.002
1.68	1.69	1.66	1.68	0.00	0.00	0.00	1.63	1.65	4.699
				0.21	0.19	0.16	0.00	0.00	0.048
0.00	0.00	0.00	0.00	0.00	0.00	0.00	0.00	0.00	0.002
0.00	0.00	0.00	0.00	0.00	0.00	0.00	0.02	0.00	0.002
0.00	0.01	0.00	0.01	0.00	0.00	0.00	0.00	0.00	0.003
							0.27	0.30	0.000
							0.04	0.00	0.265
0.83	0.83	0.83	0.84				0.84	0.85	0.95
			$\begin{array}{cccccccccccccccccccccccccccccccccccc$						

^bIntercumulus ^cOrthopyroxene inner corona ^{*}Calculated

IV

Table B.2 – Microprobe analysis from sample BLA-14 and BLA-15. Oxides are in wt% and minerals are normalized to relevant number of oxygen.

Sample				BLA-14	-14					BLA-15	-15	
Mineral	Ol^a	Ol^{a}	Ol^{a}	Ol^{a}	Opx^c	Am	Am	Am	Ol^{a}	Am	Am	Am
Point	115/1	116/1	1/2	9/2	119/1	120/1	124/1	14/2	111/1	112/1	113/1	114/1
SiO_2	39.74	39.91	39.85	39.59	56.16	42.38	42.57	42.16	39.74	45.12	44.55	44.39
Al ₂ O ₃	0.00	0.00	0.00	0.00	1.03	16.91	17.41	17.92	0.00	16.44	16.57	19.77
CaO	0.00	0.02	0.00	0.03	0.24	12.00	12.06	12.02	0.00	12.04	12.04	0.62
FeO	15.50	15.54	15.66	15.58					15.50			
MnO	0.18	0.20	0.24	0.21	0.27	0.10	0.08	0.13	0.18	0.09	0.01	0.16
Cr_2O3	0.01	0.00	0.04	0.00	0.00	0.00	0.03	0.00	0.01	0.00	0.00	0.00
MgO	44.66	44.64	44.48	44.26	32.41	16.91	16.81	16.69	44.66	15.67	15.57	21.28
Na_2O	0.00	0.00	0.00	0.00	0.01	3.25	3.42	3.41	0.00	1.80	1.78	2.00
K_2O	0.00	0.00	0.00	0.00	0.01	0.32	0.32	0.38	0.00	0.13	0.14	0.00
TiO_2	0.01	0.00	0.01	0.00	0.00	0.09	0.08	0.09	0.01	0.28	0.35	0.13
NiO	0.23	0.16	0.20	0.19	0.05	0.03	0.04	0.05	0.23	0.08	0.07	0.08
FeO*					8.65	0.04	0.43	0.28		1.37	1.26	9.02
$Fe_2O_3^*$					1.81	5.57	5.52	5.16		4.98	5.35	0.00
Total	100.32	100.47	100.47	99.85		97.59	98.78	98.30	100.32	97.99	97.69	97.47
Si	0.99	0.99	0.99	0.99	1.96	5.99	5.96	5.93	0.99	6.30	6.25	6.15
Al	0.00	0.00	0.00	0.00	0.04	2.82	2.87	2.97	0.00	2.71	2.74	3.23
Ca	0.00	0.00	0.00	0.00	0.01	1.82	1.81	1.81	0.00	1.80	1.81	0.09
Ре	0.33	0.33	0.33	0.33					0.33			
Mn	0.00	0.00	0.01	0.00	0.01	0.01	0.01	0.02	0.00	0.01	0.00	0.02
Cr	0.00	0.00	0.00	0.00	0.00	0.00	0.00	0.00	0.00	0.00	0.00	0.00
Mg	1.68	1.68	1.67	1.67	1.69	3.57	3.51	3.50	1.68	3.26	3.25	4.39
Na	0.00	0.00	0.00	0.00	0.00	0.89	0.93	0.93	0.00	0.49	0.48	0.54
K	0.00	0.00	0.00	0.00	0.00	0.06	0.06	0.07	0.00	0.02	0.03	0.00
Ti	0.00	0.00	0.00	0.00	0.00	0.01	0.01	0.01	0.00	0.03	0.04	0.01
Ni	0.00	0.00	0.00	0.00	0.00	0.00	0.00	0.01	0.00	0.01	0.01	0.01
Fe^{2+}					0.25	0.01	0.05	0.03		0.16	0.15	1.05
Fe^{3+}					0.05	0.59	0.58	0.55		0.52	0.56	0.00
X_{Mg}	0.84	0.84	0.84	0.84	0.85	0.86	0.85	0.86	0.84	0.83	0.82	0.81
^a Cumulus ^b Intercumulus ^c Orthopyroxen	s nulus roxene of	^a Cumulus ^b Intercumulus ^c Orthopyroxene of inner olivine corona	ine corona	ದ								
*Calculated	ted											

* Calculated	^c Orthopyroxene
	ne of
	inne

aer olivine corona

^bIntercumulus

^a Cumulu	X_{Mg}	Fe^{3+}	Fe^{2+}	Ni	Ti	К	N_{a}	Mg	Cr	Mn	Fe	C_{a}	Al	Si:	Total	$Fe_2O_3^*$	FeO*	NiO	TiO_2	K_2O	Na_2O	MgO	Cr_2O_3	MnO	FeO	CaO	Al_2O_3	SiO_2	Point	Mineral	Sample
		0.39					0.79	3.50	0.00	0.01		1.91	2.75	6.10	97.62	3.66	1.90	0.12	0.11	0.17	2.88	16.58	0.00	0.06		12.56	16.46	43.11	95/1	Am	
	0.86	0.23	0.35		0.04	0.03	0.79	3.50	0.01	0.01		1.93	2.70	6.15	97.45	2.18	2.96	0.07	0.41	0.17	2.87	16.55	0.07	0.05		12.66	16.12	43.35	98/1	Am	
	0.82	0.36	0.35	0.01	0.02	0.05	0.77	3.31	0.00	0.01		1.84	2.81	6.14	98.07	3.36	2.94	0.08	0.23	0.25	2.83	15.72	0.00	0.08		12.20	16.87	43.50	100/1	Am	BLA-16
	0.91	0.04	0.05	0.00	0.00	0.00	0.02	0.91	0.01	0.00		0.96	0.06	1.95	100.88	1.40	1.59	0.00	0.11	0.00	0.27	16.82	0.23	0.08		24.88	1.39	54.09	97/1	Cpx^b	
	0.88	0.01	0.11	0.00	0.00	0.00	0.03	0.86	0.00	0.00		0.94	0.08	1.96	100.46	0.21	3.77	0.00	0.18	0.00	0.36	15.91	0.00	0.12		24.02	1.98	53.91	105/1	Cpx^b	
	0.83			0.01	0.00	0.00	0.00	1.65	0.00	0.00	0.35	0.00	0.00	0.99	100.38			0.60	0.00	0.00	0.00	43.70	0.06	0.14	16.38	0.00	0.00	39.50	76/1	Ola	
	0.83			0.01	0.00	0.00	0.00	1.65	0.00	0.00	0.35	0.00	0.00	0.99	100.51			0.55	0.00	0.00	0.00	43.78	0.01	0.15	16.42	0.02	0.02	39.57	77/1	Ol^a	
	0.83			0.01	0.00	0.00	0.00	1.65	0.00	0.00	0.35	0.00	0.00	0.99	99.84			0.70	0.00	0.00	0.00	43.43	0.02	0.12	16.37	0.02	0.01	39.15	81/1	Ola	
	0.82			0.02	0.00	0.00	0.00	1.64	0.00	0.00	0.35	0.00	0.00	1.00	99.79			0.79	0.00	0.00	0.01	42.99	0.00	0.15	16.36	0.00	0.00	39.48	82/1	Ola	
				0.00	0.00	0.00	0.15	0.00	0.00	0.00	0.00	0.88	1.85	2.13	100.86			0.00	0.00	0.02	1.71	0.01	0.01	0.00	0.01	17.92	34.23	46.95	89/1	$\mathbf{Pl}^{\mathbf{a}}$	BLA-17
				0.00	0.00	0.00	0.14	0.00	0.00	0.00	0.00	0.89	1.87	2.11	100.42			0.01	0.00	0.01	1.52	0.00	0.00	0.00	0.08	18.01	34.46	46.33	94/1	$\mathbf{Pl}^{\mathbf{a}}$	
	0.84	0.00	0.31	0.00	0.00	0.00	0.00	1.65	0.00	0.01		0.01	0.03	1.99	100.66	0.00	10.64	0.07	0.02	0.01	0.00	31.72	0.03	0.22		0.19	0.73	57.03	80/1	Opx^c	
	0.84	0.04	0.28	0.00	0.00	0.00	0.00	1.67	0.00	0.01		0.01	0.03	1.97	100.09	1.33	9.60	0.10	0.03	0.01	0.00	31.87	0.01	0.20		0.25	0.65	56.04	85/1	Opx^c	
	0.83	0.15	0.51	0.01	0.23	0.12	0.71	3.34	0.05	0.01		1.86	2.61	6.10	97.10	1.43	4.26	0.08	2.10	0.65	2.54	15.59	0.41	0.09		12.08	15.41	42.46	92/1	Am	

to relevant number of oxygen. Table B.3 – Microprobe analysis from sample BLA-16 and BLA-17. Oxides are in wt% and minerals are normalized

T

VI

Table B.4 – Microprobe analysis from sample BLA-18, BLA-19 and BLA-20. Oxides are in wt% and minerals are normalized to relevant number of oxygen.

	Cpx^b	22/2	51.96	3.61	22.97		0.08	0.62	15.96	0.82	0.02	1.09	0.01	1.32	2.39	100.85	1.88	0.15	0.89		0.00	0.02	0.86	0.06	0.00	0.03	0.00	0.04	0.07	0.89	
	$\mathrm{Opx}^{\mathrm{c}}$	18/2	56.40	1.29	0.25		0.23	0.00	31.64	0.00	0.00	0.00	0.05	10.45	0.26	100.57	1.97	0.05	0.01		0.01	0.00	1.65	0.00	0.00	0.00	0.00	0.31	0.01	0.84	
-20	Ol^{a}	20/2	39.73	0.00	0.00	16.17	0.23	0.00	44.17	0.00	0.00	0.00	0.26			100.56	0.99	0.00	0.00	0.34	0.00	0.00	1.66	0.00	0.00	0.00	0.01			0.83	
BLA-20	Ol^a	19/2	39.79	0.00	0.00	16.24	0.25	0.03	44.17	0.00	0.00	0.00	0.24			100.73	0.99	0.00	0.00	0.34	0.01	0.00	1.66	0.00	0.00	0.00	0.00			0.83	
	Ol^{a}	16/2	39.61	0.00	0.03	16.43	0.26	0.03	43.55	0.00	0.01	0.03	0.20			100.13	0.99	0.00	0.00	0.35	0.01	0.00	1.65	0.00	0.00	0.00	0.00			0.83	
	Ol^{a}	15/2	39.81	0.01	0.04	16.24	0.23	0.00	43.74	-0.01	0.00	0.02	0.25			100.33	1.00	0.00	0.00	0.34	0.01	0.00	1.65	0.00	0.00	0.00	0.01			0.83	
	$\mathrm{Opx}^{\mathrm{c}}$	32/2	56.30	1.53	0.19		0.24	0.03	31.53	0.00	0.00	0.00	0.03	10.60	0.11	100.57	1.97	0.06	0.01		0.01	0.00	1.64	0.00	0.00	0.00	0.00	0.31	0.00	0.84	
BLA-19	Ol^{a}	33/2	39.65	0.01	0.00	16.61	0.22	0.01	44.03	0.01	0.01	0.02	0.19			100.76	0.99	0.00	0.00	0.35	0.00	0.00	1.66	0.00	0.00	0.00	0.00			0.83	
	Ol^{a}	32/2	40.01	0.02	0.01	16.30	0.23	0.01	43.83	0.02	0.00	0.05	0.18			100.67	1.00	0.00	0.00	0.34	0.01	0.00	1.65	0.00	0.00	0.00	0.00			0.83	
	$^{\mathrm{Am}}$	30/2	45.99	12.14	12.35		0.07	0.19	17.73	2.07	0.23	0.68	0.02	1.13	5.42	98.01	6.46	2.01	1.86		0.01	0.02	3.72	0.56	0.04	0.07	0.00	0.13	0.57	0.84	
	Am	26/2	45.79	12.22	12.18		0.10	0.32	18.17	2.04	0.27	0.58	0.05	0.00	6.47	98.18	6.42	2.02	1.83		0.01	0.03	3.80	0.56	0.05	0.06	0.01	0.00	0.68	0.85	đ
BLA-18	Ol^{a}	31/2	40.04	0.04	0.02	15.07	0.26	0.01	44.81	0.00	0.01	0.00	0.25			100.49	0.99	0.00	0.00	0.32	0.01	0.00	1.68	0.00	0.00	0.00	0.00			0.84	aner olivine corona
	Ol^{a}	24/2	39.51	0.00	0.04	14.94	0.21	0.00	45.38	0.00	0.00	0.00	0.23			100.32	0.98	0.00	0.00	0.31	0.00	0.00	1.71	0.00	0.00	0.00	0.00			0.84	inner oliv
	Ol^{a}	23/2	39.50	0.01	0.00	14.93	0.21	0.00	45.08	0.00	0.00	0.03	0.31			100.06	0.99	0.00	0.00	0.32	0.00	0.00	1.70	0.00	0.00	0.00	0.01			0.84	^a Cumulus ^b Intercumulus ^c Orthopyroxene of ii
Sample	Mineral	Point	SiO_2	Al_2O_3	CaO	FeO	MnO	Cr_2O_3	MgO	Na_2O	K_2O	TiO_2	NiO	FeO*	$Fe_2O_3^*$	Total	Si	Al	Са	Fe	Mn	Cr	Mg	Na	K	Ti	Ni	Fe^{2+}	Fe^{3+}	X_{Mg}	^a Cumulus ^b Intercumulus ^c Orthopyroxer

VII

number of oxygen. Table B.5 - Microprobe analysis from sample BLA-21. Oxides are in wt% and minerals are normalized to relevant

C									
Sample	Ola	Ola	Ola	÷ .	DIA-21	Dla	On c	C b	>
Doint	1 /1	ې 1/2	17/1	10/1	19/1	19/1	/1/1	r/ a	16/1
SiO_2	39.23	39.14	39.40	39.07	47.35	47.48	55.79	51.42	41.86
Al_2O_3	0.00	0.00	0.00	0.01	33.76	33.04	1.06	3.40	17.30
$C_{a}O$	0.01	0.01	0.00	0.00	17.13	16.87	0.18	23.48	11.88
FeO	17.13	17.12	17.40	17.40	0.06	0.00			
MnO	0.22	0.24	0.22	0.23	0.00	0.00	0.30	0.14	0.03
Cr_2O_3	0.00	0.00	0.00	0.01	0.00	0.00	0.04	0.77	0.00
MgO	43.47	43.28	43.44	43.25	0.00	0.00	31.41	15.71	15.93
Na_2O	0.00	0.00	0.00	0.00	2.01	2.23	0.01	0.58	3.08
K_2O	0.00	0.00	0.01	0.01	0.03	0.02	0.00	0.00	0.73
TiO_2	0.00	0.00	0.00	0.00	0.02	0.02	0.05	0.86	1.27
NiO	0.20	0.16	0.29	0.14	0.02	0.00	0.06	0.05	0.04
FeO*							10.12	1.30	2.47
$Fe_2O_3^*$							1.04	2.05	3.29
Total	100.27	99.96	100.76	100.12	100.36	99.66	100.06	99.77	97.87
Si	0.99	0.99	0.99	0.99	2.16	2.18	1.96	1.88	5.94
Al	0.00	0.00	0.00	0.00	1.83	1.81	0.04	0.15	2.89
C_{a}	0.00	0.00	0.00	0.00	0.85	0.84	0.01	0.92	1.81
Fe	0.36	0.37	0.37	0.37	0.00	0.00			
Mn	0.00	0.01	0.00	0.00	0.00	0.00	0.01	0.00	0.00
$\Omega_{\mathbf{r}}$	0.00	0.00	0.00	0.00	0.00	0.00	0.00	0.02	0.00
Mg	1.65	1.65	1.64	1.65	0.00	0.00	1.65	0.86	3.37
N_{a}	0.00	0.00	0.00	0.00	0.18	0.20	0.00	0.04	0.85
К	0.00	0.00	0.00	0.00	0.00	0.00	0.00	0.00	0.13
Ti	0.00	0.00	0.00	0.00	0.00	0.00	0.00	0.02	0.14
Ni	0.00	0.00	0.01	0.00	0.00	0.00	0.00	0.00	0.00
Fe^{2+}							0.30	0.04	0.29
Fe_{3+}							0.03	0.06	0.35
X_{Mg}	0.82	0.82	0.82	0.82			0.84	0.90	0.84
^a Cumulus									
^b Intercumulus	nulus								

° Intercum

^cOrthopyroxene of inner olivine corona ^{*}Calculated

VIII

 $Table \ B.6$ – Microprobe analysis from sample BLA-22. Oxides are in wt% and minerals are normalized to relevant number of oxygen.

Sample							BLA-22						
Mineral	Ol^a	Ol^a	Ol^a	Pla	Pl^{a}	Pl^{a}	Pl^{a}	Pl^{a}	Cpx^b	Opx^{c}	Cpx^b	Opx^{c}	Am
Point	34/1	39/1	40/1	44/1	45/1	19/1	20/1	27/1	43/1	47/1	22/1	24/1	46/1
SiO_2	39.73	39.40	39.37	47.09	47.25	46.92	46.69	47.07	51.54	54.51	51.44	56.89	43.09
Al_2O_3	0.01	0.00	0.00	33.52	33.50	33.64	33.93	34.22	3.68	3.77	3.10	0.83	14.18
CaO	0.03	0.00	0.01	17.39	17.03	17.47	17.76	17.57	23.45	0.16	23.70	0.22	12.32
FeO	16.34	16.85	16.80	0.01	0.09	0.02	0.07	0.04					
MnO	0.18	0.19	0.20	0.01	0.00	0.00	0.02	0.00	0.16	0.05	0.09	0.27	0.07
Cr_2O_3	0.00	0.01	0.00	0.02	0.00	0.02	0.00	0.00	0.62	0.04	0.76	0.02	0.44
MgO	43.92	43.52	43.73	0.00	0.00	0.02	0.00	0.00	15.03	25.60	15.34	31.85	16.23
Na_2O	0.00	0.03	0.00	1.93	2.00	1.84	1.77	1.77	0.77	0.14	0.68	0.00	2.85
$\mathbf{K}_{2}\mathbf{O}$	0.02	0.00	0.00	0.02	0.01	0.01	0.01	0.01	0.00	0.04	0.00	0.00	0.72
TiO_2	0.00	0.02	0.00	0.02	0.06	0.01	0.05	0.02	1.09	0.02	1.05	0.00	2.08
NiO	0.26	0.23	0.23	0.00	0.00	0.00	0.00	0.02	0.03	0.02	0.03	0.06	0.10
FeO*									2.02	9.97	1.47	10.66	5.08
$Fe_2O_3^*$									1.79	0.00	2.44	0.47	0.76
Total	100.50	100.25	100.34	100.01	99.95	99.96	100.30	100.71	100.17	94.31	100.10	101.26	97.91
is.	0.99	0.99	66.0	2.15	2.16	2.15	2.13	2.14	1 88.1	2.06	1.88	1.98	6.16
A1	0.00	0.00	0.00	1.83	1.83	1.84	1.85	1.85	0.16	0.17	0.13	0.03	2.39
Ca Da	0.00	0.00	0.00	0.86	0.84	0.87	0.88	0.86	0.92	0.01	0.93	0.01	1.89
Fe	0.35	0.36	0.36	0.00	0.00	0.00	0.00	0.00					
Mn	0.00	0.00	0.00	0.00	0.00	0.00	0.00	0.00	0.01	0.00	0.00	0.01	0.01
Cr	0.00	0.00	0.00	0.00	0.00	0.00	0.00	0.00	0.02	0.00	0.02	0.00	0.05
Mg	1.66	1.65	1.66	0.00	0.00	0.00	0.00	0.00	0.82	1.44	0.84	1.65	3.46
Na	0.00	0.00	0.00	0.17	0.18	0.17	0.16	0.16	0.05	0.01	0.05	0.00	0.79
К	0.00	0.00	0.00	0.00	0.00	0.00	0.00	0.00	0.00	0.00	0.00	0.00	0.13
Ţi	0.00	0.00	0.00	0.00	0.00	0.00	0.00	0.00	0.03	0.00	0.03	0.00	0.22
Ni	0.01	0.00	0.00	0.00	0.00	0.00	0.00	0.00	0.00	0.00	0.00	0.00	0.01
Fe^{2+}									0.06	0.31	0.05	0.31	0.61
Fe^{3+}									0.05	0.00	0.07	0.01	0.08
X_{Mg}	0.83	0.82	0.82						0.88	0.82	0.88	0.84	0.83
^a Cumulus ^b Intercumulus	ıs mulus												
^c Orthopy	^c Orthopyroxene of inner olivine corona	inner oliv	ine corona	5									
*Calculated	ted												

B.2 Hydrous minerals

Table B.7 – Microprobe analysis from sample BLA-13 and BLA-14. Oxides are in wt% and minerals are normalized to relevant number of oxygen.

							_									_										-
	Spt	10/2	39.59	0.00	0.03	15.58	0.21	0.00	44.26	0.00	0.00	0.00	0.19	99.85	1.74	0.00	0.00	0.58	0.01	0.00	2.93	0.00	0.00	0.00	0.01	
	Spt	5/2	41.03	0.34	0.06	6.77	0.04	0.00	39.39	0.00	0.01	0.02	0.17	87.84	1.94	0.02	0.00	0.27	0.00	0.00	2.81	0.00	0.00	0.00	0.01	000
3LA-14	$_{\mathrm{Spt}}$	4/2	41.82	1.70	0.05	6.16	0.10	0.03	38.59	0.00	0.00	0.01	0.04	88.49	1.95	0.09	0.00	0.24	0.00	0.00	2.71	0.00	0.00	0.00	0.00	
		118/1													1.90	0.08	0.00	0.28	0.00	0.00	2.77	0.00	0.00	0.00	0.00	0
	Spt	117/1	41.52	1.55	0.49	11.69	0.28	0.03	30.27	0.03	0.00	0.01	0.08	85.95	2.04	0.09	0.03	0.49	0.01	0.00	2.25	0.00	0.00	0.00	0.00	
	Pmp	74/1	37.24	26.59	23.30	4.07	0.37	0.00	1.32	0.07	0.01	0.02	0.00	92.98	2.92	2.48	1.98	0.27	0.02	0.00	0.16	0.01	0.00	0.00	0.00	
	Pmp	62/1	37.06	26.46	23.14	2.18	0.12	0.03	3.82	0.04	0.01	0.00	0.02	92.86	2.88	2.45	1.95	0.14	0.01	0.00	0.45	0.01	0.00	0.00	0.00	
	Pmp	59/1	36.83	27.05	23.43	2.61	0.05	0.00	2.12	0.06	0.00	0.00	0.04	92.19	2.89	2.53	1.99	0.17	0.00	0.00	0.25	0.01	0.00	0.00	0.00	
	$_{\mathrm{Spt}}$	71/1	51.11	0.21	0.14	2.61	0.04	0.03	35.75	0.01	0.03	0.05	0.24	90.22	2.25	0.01	0.01	0.10	0.00	0.00	2.37	0.00	0.00	0.00	0.01	000
v-13	Spt	70/1	44.26	0.24	0.26	5.17	0.03	0.02	35.14	0.01	0.05	0.06	0.00	85.23	2.11	0.01	0.01	0.21	0.00	0.00	2.53	0.00	0.00	0.00	0.00	
BLA	Spt	/1 66 $/1$ 70 $/$	44.10	2.45	0.37	9.13	0.09	0.00	29.11	0.02	0.04	0.02	0.00	85.35	2.13	0.14	0.02	0.37	0.00	0.00	2.12	0.00	0.00	0.00	0.00	70.0
	$_{\mathrm{Spt}}$	65/1	42.55	3.01	0.37	9.42	0.06	0.02	29.54	0.02	0.02	0.04	0.03	85.09	2.07	0.18	0.02	0.39	0.00	0.00	2.17	0.00	0.00	0.00	0.00	700
	$_{\mathrm{Spt}}$	56/1	40.83	0.02	0.02	5.48	0.02	0.03	39.97	0.00	0.00	0.00	0.21	86.57	1.95	0.00	0.00	0.22	0.00	0.00	2.87	0.00	0.00	0.00	0.01	000
	Spt	52/1	48.42	6.56	0.20	6.91	0.03	0.01	28.15	0.11	0.05	0.00	0.09	90.54	2.15	0.35	0.01	0.26	0.00	0.00	1.89	0.01	0.00	0.00	0.00	00 0
	Spt	51/1	56.79	3.15	0.46	4.93	0.01	0.00	26.51	0.02	0.04	0.00	0.29	92.22	2.42	0.16	0.02	0.18	0.00	0.00	1.71	0.00	0.00	0.00	0.01	10.0
Sample	Mineral	Point	SiO_2	Al_2O_3	CaO	FeO	MnO	Cr_2O_3	MgO	Na_2O	K_2O	TiO_2	NiO	Total	Si	Al	Ca	Fe	Mn	Cr	Mg	Na	К	Ti	Ni	

to relevant number of oxygen.	Table B.8 - Microprobe analysis from sample BLA-16 and BLA-17. Oxides are in wt% and
	Oxides are in wt% and minerals are normalized

Sample					BLA-16							BLA-17		
Mineral	Spt	$_{\rm Spt}$	Spt	Spt	Prn	\mathbf{Prn}	Prn	Prn	Chl	$_{\rm Spt}$	Spt	Spt	Spt	\mathbf{Prn}
Point	10/2	96/1	99/1	101/1	102/1	103/1	107/1	109/1	110/1	78/1	83/1	84/1	91/1	88/1
SiO_2	39.59	32.68	36.11	35.99	43.48	43.17	43.08	43.00	37.47	43.50	45.02	41.12	33.57	43.43
Al_2O_3	0.00	15.50	13.81	13.51	24.17	24.26	23.49	24.38	12.65	0.00	0.01	1.55	14.54	24.52
CaO	0.03	0.21	0.51	0.53	27.43	26.05	25.75	27.60	0.22	0.18	0.13	0.11	0.34	27.59
FeO	15.58	9.93	3.26	3.65	0.05	0.14	0.10	0.02	2.44	8.76	8.03	10.50	10.73	0.02
MnO	0.21	0.29	0.18	0.25	0.06	0.11	0.04	0.04	0.16	0.07	0.00	0.04	0.32	0.00
Cr_2O_3	0.00	0.00	0.05	0.00	0.00	0.00	0.01	0.00	0.01	0.00	0.00	0.02	0.04	0.01
MgO	44.26	26.98	31.43	31.51	0.31	1.53	0.01	0.00	33.20	33.56	32.88	32.91	25.90	0.01
Na_2O	0.00	0.02	0.02	0.02	0.04	0.01	0.03	0.02	0.06	0.01	0.00	0.00	0.00	0.00
K_2O	0.00	0.02	0.00	0.03	0.00	0.00	0.02	0.01	0.03	0.02	0.04	0.03	0.04	0.02
TiO_2	0.00	0.00	0.02	0.03	0.00	0.01	0.06	0.01	0.02	0.01	0.00	0.01	0.02	0.01
NiO	0.19	0.14	0.03	0.03	0.04	0.00	0.00	0.02	0.06	0.20	0.08	0.00	0.15	0.03
Total	99.85	85.77	85.43	85.55	95.58	95.28	92.61	95.11	86.33	86.29	86.19	86.28	85.66	95.63
Si	1.74	1.60	1.71	1.71	2.98	2.96	3.03	2.96	6.98	2.09	2.15	2.00	1.65	2.97
A1	0.00	0.91	0.78	0.76	1.97	1.98	1.97	2.00	2.81	0.00	0.00	0.09	0.85	2.00
C_a	0.00	0.01	0.03	0.03	2.04	1.94	1.96	2.06	0.04	0.01	0.01	0.01	0.02	2.05
Fe	0.58	0.41	0.13	0.15	0.00	0.01	0.01	0.00	0.38	0.36	0.32	0.43	0.45	0.00
Mn	0.01	0.01	0.01	0.01	0.00	0.01	0.00	0.00	0.03	0.00	0.00	0.00	0.01	0.00
Ωr	0.00	0.00	0.00	0.00	0.00	0.00	0.00	0.00	0.00	0.00	0.00	0.00	0.00	0.00
Mg	2.93	1.99	2.24	2.25	0.03	0.16	0.00	0.00	9.33	2.44	2.37	2.42	1.92	0.00
Na	0.00	0.00	0.00	0.00	0.01	0.00	0.00	0.00	0.02	0.00	0.00	0.00	0.00	0.00
К	0.00	0.00	0.00	0.00	0.00	0.00	0.00	0.00	0.01	0.00	0.00	0.00	0.00	0.00
Ti	0.00	0.00	0.00	0.00	0.00	0.00	0.00	0.00	0.00	0.00	0.00	0.00	0.00	0.00
Ni	0.01	0.01	0.00	0.00	0.00	0.00	0.00	0.00	0.01	0.01	0.00	0.00	0.01	0.00
X_{Mg}	0.84	0.83	0.94	0.94	0.91	0.95	0.10	0.00	0.96	0.87	0.88	0.85	0.81	0.31

Table B.9 – Microprobe analysis from sample BLA-18, BLA-20 and BLA-21. Oxides are in wt% and minerals are normalized to relevant number of oxygen.

_															 											
	Pmp	14/1	37.28	26.88	23.31	4.58	0.20	0.00	1.11	0.04	0.01	0.03	0.00	93.44	2.91	2.50	1.97	0.30	0.01	0.00	0.13	0.01	0.00	0.00	0.00	0.30
BLA-21	Pmp	9/1	35.96	27.32	22.99	5.15	0.39	0.00	0.62	0.04	0.02	0.03	0.00	92.54	2.85	2.58	1.97	0.35	0.03	0.00	0.07	0.01	0.00	0.00	0.00	0.18
	Spt	5/1	40.91	0.09	0.02	4.60	0.00	0.01	41.19	0.01	0.01	0.00	0.17	87.00	1.93	0.00	0.00	0.18	0.00	0.00	2.94	0.00	0.00	0.00	0.01	0.94
-20	$_{\rm Spt}$	21/2	42.86	0.34	0.04	6.75	0.09	0.00	36.40	0.00	0.00	0.03	0.02	86.54	2.04	0.02	0.00	0.27	0.00	0.00	2.61	0.00	0.00	0.00	0.00	0.91
BLA-20	$_{\rm Spt}$	17/2	43.09	0.82	0.15	5.88	0.12	0.04	36.46	0.01	0.02	0.02	0.02	86.63	2.04	0.05	0.01	0.24	0.00	0.00	2.60	0.00	0.00	0.00	0.00	0.92
	Chl	28/2	29.86	20.42	0.03	4.74	0.04	0.42	30.86	0.00	0.00	0.10	0.16	86.64	 5.66	4.62	0.01	0.76	0.01	0.06	8.83	0.00	0.00	0.02	0.02	0.92
BLA-18	$_{\rm Spt}$	27/2	37.95	2.68	0.12	10.75	0.20	0.09	33.13	0.03	0.01	0.08	0.03	85.07	1.89	0.16	0.01	0.45	0.01	0.00	2.49	0.00	0.00	0.00	0.00	0.85
	$_{\rm Spt}$	25/2	41.55	0.51	0.13	7.38	0.12	0.00	36.35	0.01	0.00	0.00	0.26	86.32	2.00	0.03	0.01	0.30	0.01	0.00	2.64	0.00	0.00	0.00	0.01	0.90
Sample	Mineral	Point	SiO_2	Al_2O_3	CaO	FeO	MnO	Cr_2O_3	MgO	Na_2O	$\rm K_2O$	TiO_2	NiO	Total	Si	Al	Ca	Fe	Mn	\mathbf{Cr}	Mg	Na	К	Ti	Ni	\mathbf{X}_{Mg}

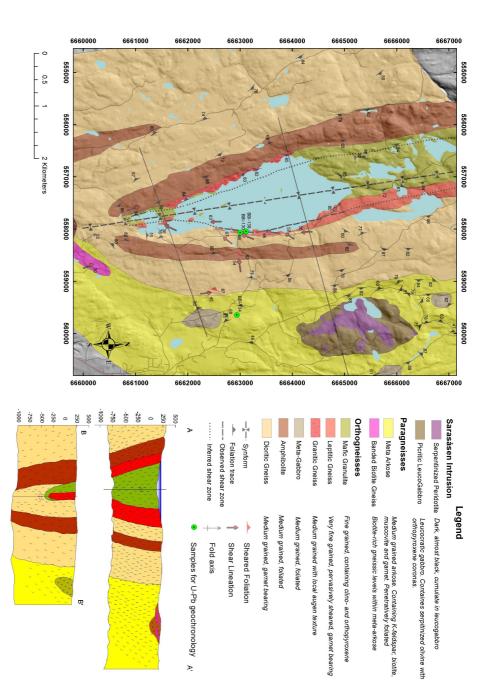
number	Table
er of oxygen.	Table B.10 -
ten.	Microprobe analysis from sample BLA-22. Oxides are in wt% and mi
	analysis
	sis from
	sample
	BLA - 22 .
	Oxides
	are i
	in wt%
	and
	inerals
	are
	normalized
	to relevant

X_{Mg}	Ni	Ţ.	K	N_{a}	Mg	Q	Mn	Fe	C_{a}	Al	Si:	Total	NiO	$\rm TiO_2$	K_2O	Na_2O	MgO	Cr_2O_3	MnO	FeO	$C_{a}O$	Al_2O_3	SiO2	Point	Mineral	Sample
0.81	0.00	0.00	0.00	0.01	1.82	0.00	0.00	0.43	0.01	0.40	2.06	89.03	0.03	0.00	0.04	0.11	26.04	0.03	0.04	10.83	0.17	7.30	44.45	23/1	$_{\rm Spt}$	
0.54	0.02	0.00	0.01	0.00	0.86	0.00	0.00	0.74	0.09	0.07	2.59	85.61	0.42	0.07	0.12	0.03	11.57	0.00	0.06	17.86	1.62	1.12	52.73	35/1	Spt	
0.82	0.00	0.00	0.00	0.00	2.02	0.00	0.01	0.45	0.04	0.30	2.01	84.13	0.06	0.03	0.04	0.01	26.82	0.00	0.20	10.78	0.75	5.12	40.34	38/1	Spt	
0.31	0.00	0.00	0.00	0.01	0.11	0.00	0.02	0.24	1.98	2.57	2.89	92.30	0.00	0.03	0.00	0.05	0.94	0.03	0.25	3.66	23.21	27.35	36.79	21/1	Pmp	
0.91	0.02	0.00	0.01	0.00	5.41	0.00	0.00	0.54	0.02	0.11	7.92	93.45	0.15	0.00	0.03	0.00	27.30	0.03	0.01	4.82	0.14	0.67	60.29	25/1	Tlc	BLA-22
0.93	0.01	0.00	0.00	0.00	5.62	0.00	0.00	0.44	0.02	0.10	7.88	94.55	0.10	0.01	0.02	0.01	28.75	0.00	0.00	4.01	0.11	0.66	60.89	26/1	Tlc	
0.89	0.01	0.00	0.00	0.00	5.27	0.00	0.01	0.63	0.20	0.10	7.86		0.12	0.02	0.01	0.01	26.23	0.02	0.05	5.60	1.38	0.60	59.01	33/1	Tlc	
0.91	0.02	0.00	0.01	0.01	5.31	0.00	0.00	0.50	0.05	0.24	7.87		0.15	0.01	0.04	0.02	26.72	0.02	0.03	4.52	0.36	1.53	59.82	48/1	Tlc	
0.91	0.01	0.00	0.00	0.01	5.22	0.00	0.00	0.54	0.06	0.26	7.88		0.06	0.02	0.02	0.02	26.12	0.02	0.03	4.82	0.45	1.67	59.56	49/1	Tlc	

B.3 Geological Map

This is for illustrative purposes only. A high-resolution map is provided as a separate appendix.

Figure B.1 - Geological map of Væleren - Sarasåsen



XVI